Orbital tuning for the middle Eocene to early Oligocene Monte Cagnero Section (central Italy): paleoenvironmental and paleoclimatic implications

Marcus V. L. Kochhann[1,*], Jairo F. Savian[2], Flavia Tori[3], Rita Catanzariti[4], Rodolfo Coccioni[5], Fabrizio Frontalini[6], Luigi Jovane[7], Fabio Florindo[8], Simonetta Monechi[3,9]

[1]Programa de Pós-Graduação em Geociências, Universidade Federal do Rio Grande do Sul, Av. Bento Gonçalves 9500, 91501-970, Porto Alegre, Brazil

[2]Departamento de Geologia, Instituto de Geociências, Universidade Federal do Rio Grande do Sul, Av. Bento Gonçalves 9500, 91501-970, Porto Alegre, Brazil

[3]Dipartimento di Scienze della Terra, Università di Firenze, Via la Pira 4, I-50121, Firenze, Italy

[4]Istituto di Geoscienze e Georisorse, Consiglio Nazionale delle Ricerche (CNR), 56124, Pisa, Italy

[5]Università degli Studi di Urbino "Carlo Bo", Campus Scientifico, Località Crocicchia, 61029, Urbino, Italy

[6]Dipartimento di Scienze Pure e Applicate, Università degli Studi di Urbino "Carlo Bo", Campus Scientifico, Località Crocicchia, 61029, Urbino, Italy

[7]Departamento de Oceanografia Física, Química e Geológica, Instituto Oceanográfico, Universidade de São Paulo, Praça do Oceanográfico 191, 05508-120, São Paulo, Brazil

[8]Istituto Nazionale di Geofisica e Vulcanologia, Via di Vigna Murata 605, 00143, Roma, Italy

[9]Institute for Climate Change Solutions, 61040, Frontone, Italy

*corresponding author: Marcus Vinicius Lermen Kochhann (marcus.kochhann@ufrgs.br)

Abstract

During the middle Eocene to early Oligocene Earth transitioned from a greenhouse to ~~the~~ icehouse climate state. The interval comprises the Middle Eocene Climatic Optimum (MECO; ~40 Ma) and a subsequent long-term cooling trend that culminated in the Eocene-Oligocene transition (EOT; ~34 Ma)~~, and~~ with the Oi-1 glaciation. Here, we present a refined calcareous nannofossil biostratigraphy and an orbitally tuned age model for the Monte Cagnero (MCA) section spanning ~~from~~ the middle Eocene to the early Oligocene (~41 to ~33 Ma). Spectral analysis of~~n~~ magnetic susceptibility (MS) data displays strong cyclicities in the orbital frequency band ~~frequency~~ allowing us to tune the identified 405 kyr ~~long~~ eccentricity minima in the MS record to ~~long eccentricity minima~~their equivalents in the astronomical solution. Our orbitally tuned age model allows us to estimate the position and duration of polarity chrons (C18 to C13) and compare them with other standard and orbitally tuned ages. We were also able to constrain the timing and duration of the MECO event, which coincides with a minimum in the 2.4 Myr and 405 kyr eccentricity cycles. Our study corroborates the previous estimated age for the base of the Rupelian stage (33.9 Ma) and estimates the base of the Priabonian stage in the MCA section to be at 37.4 Ma. Finally, calcareous nannofossils with known paleoenvironmental preferences show a general gradual shift from oligotrophic to eutrophic conditions with an abrupt change ~~dominance reversal~~ at ~37 Ma. Besides, nannofossil assemblages suggest that enhanced nutrient availability preceded water cooling at the late Eocene. Altogether, this evidence points to a poorly developed water column stratification prior to the cooling trend.

Keywords: Neo-Tethys Ocean; Astrochronology; Trophic conditions; Eocene-Oligocene boundary; MECO event

Highlights:

- Magnetic susceptibility displays imprinted orbital signals used for orbital tuning

- Orbitally tuned age model developed for the Middle Eocene to early Oligocene interval
- Refined calcareous nannofossil biostratigraphy has been established
- ~~Dominance reversal~~Abrupt change from oligotrophic to eutrophic conditions at ~37 Ma
- Poorly developed water column stratification prior to the late Eocene cooling trend

1. Introduction

The middle Eocene to early Oligocene was a key transition in Earth's climatic history represented by the shift from a greenhouse to an icehouse climate, when global climate changed from warm, comparatively ice-free conditions, to the colder, more glaciated state of the Neogene (Zachos et al., 2008). This interval is characterized by a gradual long-term cooling trend in which there is a superimposed important climatic event, known as the Middle Eocene Climatic Optimum (MECO; Bohaty and Zachos, 2003; Jovane et al., 2007a; Bohaty et al., 2009; Westerhold et al., 2020). Unlike ~~of~~ the hyperthermal events such as the Paleocene-Eocene Thermal Maximum (PETM), and the Eocene Thermal maximum 2 and 3 (ETM2 and ETM3), the MECO is ~~by~~ far ~~the~~ more controversial ~~event~~ to interpret (Bohaty and Zachos, 2003; Sluijs, 2013; Giorgioni et al., 2019). This ~500 kyr-long event, with the peak warming lasting <100 kyr and centered at ~40.0 Ma, is characterized by a global decline in oxygen isotopic ~~records~~ values ($\delta^{18}O$), being interpreted as a 4 to 6 ºC warming of bottom and surface waters, and an evident shallowing of the carbonate compensation depth (CCD; Bohaty and Zachos, 2003; Bohaty et al., 2009). Despite this warming event, the global cooling trend ~~continues~~ continued until it reached its maximum during the Eocene-Oligocene transition (EOT) at ~34.0 Ma (Jovane et al., 2007b; Westerhold et al., 2014). $\delta^{18}O$ values increase over 1.0‰ during the transition (e.g., Kennett, 1977; Zachos et al., 1996; Coxall et al., 2005) and are interpreted as an Antarctic ice-sheet growth of 60 to 110% of the present volume and a 3 to 4 ºC bottom waters cooling (Zachos et al., 1996, Lear et al., 2008). Concomitant to the onset of Antarctic glaciation, a >1 km drop in the CCD occurred (Coxall et al., 2005). Both the ice-sheet growth and the CCD deepening occurred in two pulses lasting ~40 kyr each and positioned 300 to 400 kyr apart, pointing to a probable orbital pacing (Coxall et al., 2005). The cause of this major global climate reorganization is classically interpreted to be the thermal isolation of Antarctica due to the onset of Antarctic Circumpolar current, as a consequence of the Southern Ocean gateways opening (e.g., Kennett, 1977; Kennett and Exon, 2004; Barker et al., 2007). A more recent hypothesis for a main driving factor suggests that a pCO_2 threshold was crossed (e.g., DeConto and Pollard, 2003; Ladant et al., 2014), but the reason why pCO_2 declined is yet unresolved. A possible explanation is that the Arabia-Eurasia collision and closure of the Tethys Ocean gateway triggered different mechanisms that reduced atmospheric pCO_2 (Allen and Armstrong, 2008; Jovane et al., 2009).

Astronomically driven climatic~~e~~ ~~forcing~~ fluctuations can be preserved as changes in the sediment properties within the stratigraphic record and the correlation of this cyclic variations recorded in climate proxies to astronomical models (extensively known as astronomical tuning) has become a standard tool for calibrating different epochs of the Geologic Time Scale (GTS) (e.g., Gradstein et al., 2012). The astronomical time scale (ATS) covered almost the entirely Cenozoic except for the middle-late Eocene, which is known as the middle-late Eocene gap (Hilgen et al., 2012). This is probably due to the CCD shallowing, which made carbonate-rich successions scarce for this time interval (Pälike et al., 2012). Although there are numerous studies attempting to close this gap (Jovane et al., 2010; Westerhold and Röhl, 2013; Westerhold et al., 2014, 2015; Boulila et al., 2018) there is not yet a consensus on the solution. Despite these discrepancies, recognizing Earth's astronomical cycles in sedimentary records and placing them in time by the astronomical tuning approach is yet one of the most powerful techniques due to its high temporal resolution (Hinnov, 2013). These orbital cycles can lead to changes in chemical, physical, paleontological, and sedimentological properties, and consequently, be detected in the sedimentary record by different proxies. Among all, one of the widest currently used proxy is magnetic susceptibility (MS) due to its rapid, low-cost, and non-destructive data acquisition (e.g., Kodama and Hinnov, 2014; Li et al., 2019a). Since its precursor studies, MS proved to be an effective and reliable technique for cyclostratigraphy, especially when apply to marl-limestone successions (Boulila et al., 2008a, 2008b, 2008c).

The Monte Cagnero (MCA) Section is the Global Boundary Stratotype Section and Point (GSSP) for the base of the Chattian stage (28.1 Ma; Coccioni et al., 2018). ~~Besides, i~~It comprises a pelagic carbonate succession made of marl-limestone alternations, which characterizes a similar ~~is within the same geological~~stratigraphic setting ~~as~~ with ~~the~~ those of important near sections, such as the Massignano Section, GSSP for the base of the Rupelian stage (33.9 Ma; Premoli Silva and Jenkyns, 1993) and Alano Section, recently ratified GSSP for the base of the Priabonian stage (37.7 Ma; Agnini et al., 2020). The orbital control on the MCA Section has already been demonstrated by the cyclostratigraphic analysis on the EOT interval presented by~~from~~ Hyland et al. (2009), which showed the presence of Milankovitch related cycles ~~during the EOT using~~in the $CaCO_3$ content record. Our main goal is to extend this cyclostratigraphic approach towards the base of the MCA Section covering the interval studied by Jovane et al. (2013), which spans the middle Eocene to early Oligocene, and test ~~whether or not~~whether it is a suitable candidate section for studying the time interval comprising the MECO to the EOT. Besides, another goal is to investigate paleoclimatic and paleoenvironmental changes based on calcareous nannofossils assemblages.

Here, we developed a cyclostratigraphic analysis for the MCA Section using a high-resolution magnetic susceptibility record, which spans approximately 8 Myr from Chron C18n.2r (middle Eocene) ~~into the~~to Chron C12r (early Oligocene). Constrained by a radiometric date, ~~The~~ the ~~resultant~~ cyclostratigraphic ~~framework~~ analysis allowed us to reliably~~was subsequently orbitally~~ tune~~d~~ the MS record to the ZB18a astronomical solution (Zeebe and Lourens, 2019) at the ~~long~~ 405 kyr eccentricity level. The new orbitally tuned age model together with the calcareous nannofossils data allowed us to ~~refine~~ constrain the age ~~constraints for~~of biozones, polarity chrons, and climatic events, and to discuss major paleoenvironmental changes within the studied interval.

2. Geological and stratigraphic setting

The MCA Section (43°38’50”N, 12°28’05”E; 727 meters above sea-level) is a continuous Paleogene sedimentary record preserved in the Scaglia limestone, which consists of pelagic carbonate successions of the Umbria-Marche Basin, northeastern Apennines, Italy (e.g., Coccioni et al., 2008; Hyland et al., 2009; Coccioni et al., 2013; Jovane et al., 2013; Savian et al., 2014; Coccioni et al., 2018; Fig. 1a). The studied section ranges from 58 to 128 meters stratigraphic level from the base (msl, 70 m thick) and comprises calcareous marl and marly limestone lithologies from the Scaglia Variegata and Scaglia Cinerea formations. Based on previous magnetostratigraphy (Jovane et al., 2013), the studied interval ~~is~~ correspond~~ents~~s to the middle Eocene – ~~early~~ lower Oligocene, therefore spanning Earth’s greenhouse-to-icehouse transition and ~~and~~ including important climatic events such as the MECO and the Oi-1 (Fig. 1b). The stratigraphic interval corresponding to the MECO event has been already well constrained at the MCA Section by Savian et al. (2014). The EOT on the other could not yet been reliably characterized due to the lack of $\delta^{18}O$ data. Following Hutchinson et al. (2021), we assumed here the EOT as a ~790 kyr event with its onset stratigraphically correlated to the extinction of the calcareous nannofossil *Discoaster saipanensis*. The Eocene-Oligocene boundary (EOB) is well established within the section at 114.1 msl defined by the extinction of the planktonic foraminiferal Family Hantkeninidae (Premoli Silva and Jenkyns, 1993; Coccioni et al., 2008; Hyland et al., 2009; Jovane et al., 2013).

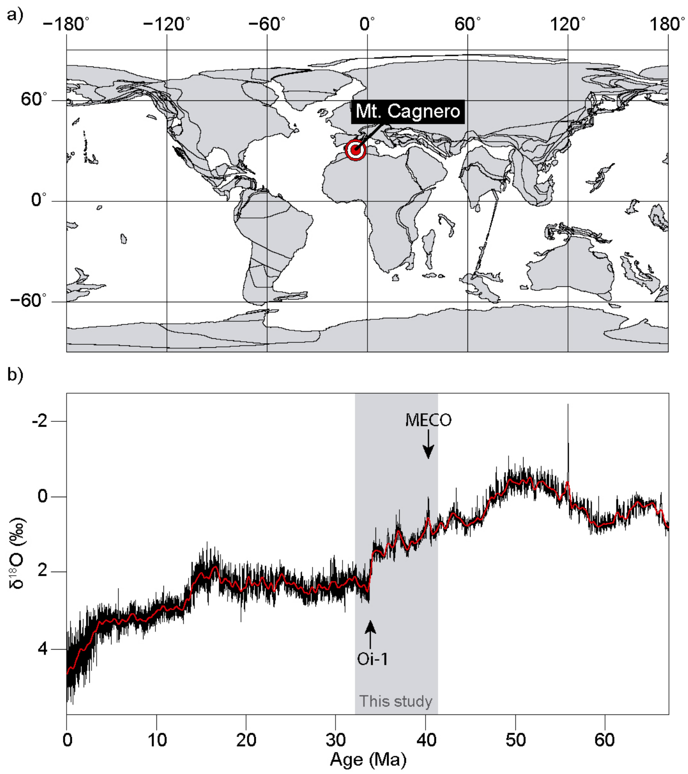

Figure 1. Paleogeographic and paleoclimate settings. a) Paleogeographic reconstruction for 35 Ma (from http://www.odsn.de) with the approximate location of the MCA Section. b) Global compilation of Cenozoic $\delta^{18}O_{benthic}$ records (Westerhold et al., 2020) with a locally weighted smooth over 1 Myr (red curve) indicating the long-term cooling, which culminated in the Oi-1 glaciation event, and the rapid warming event of the MECO superimposed on this cooling trend.

3. Material and methods

3.1. Magnetic susceptibility

Low-field mass normalized magnetic susceptibility (χ, hereafter MS) is extensively used as a paleoclimate proxy for cyclostratigraphic analyses since it is a rapid, non-destructive, and low-cost method (Kodama and Hinnov, 2014). Besides, it is considered as a reliable method for resolving ~~astronomical~~ astroclimatic cycles ~~that may be related to fine-grained terrestrial influx~~ in mixed carbonate-clay successions, once increased susceptibility implies a relative increase of ferrimagnetic and/or paramagnetic minerals associated with terrigenous detrital input (e.g., Boulila et al., 2008a, 2008b, 2008c; Kodama and Hinnov, 2014; Li et al., 2019a). The MCA interval that extends from 58 to 72 msl has MS data available with ~5 cm resolution (Savian et al., 2014). Therefore, we opted for measuring the interval between 72 to 128 msl at the same spatial resolution. MS measurements were carried out at the National Oceanography Centre Southampton (NOCS). Measurements were ~~collected~~ realized with a Kappabridge KLY-3 (AGICO) magnetic ~~susceptibility meter~~susceptometer. Combining both datasets, we generate a MS series with 1230 data points. Based on the average sediment accumulation rate (SAR) derived from magnetostratigraphy (Jovane et al., 2013), the MS series has an average temporal resolution of ~5.8 kyr.

3.2. Calcareous nannofossils

Calcareous nannofossil samples have been collected every 25 cm for the lower part of the section (58-78 msl) and every 50 cm up to 128 msl. Quantitative analyses have been performed on 180 samples. Smear slides were prepared from unprocessed samples according to standard techniques (Bown and Young, 1998) and analyzed under a polarized light microscope at a magnification of 1250X. Abundances were determined by counting 300 specimens of nannofossils in a variable number of visual fields. A supplementary counting has been performed on two traverses in order to recognize rare important biostratigraphic markers. For the biostratigraphic events recognized and the taxonomic criteria adopted we refer to Agnini et al. (2014 and references therein).

To statistically explore calcareous nannofossil data, we used a multivariate analysis approach. Principal component analysis (PCA) was performed using the PAST (PAleontological STatistics) software (Hammer et al., 2001) in order to understand major changes in calcareous nannofossil assemblages. Prior to the analysis, we grouped rare or discontinuous taxa at the genus level and excluded the remaining taxa that presented less than 0.5% of standard deviation of their relative abundances to eliminate rarely occurring species (Dunkley Jones et al., 2008). Relative abundances were then rescaled to sum to 100% and zero values were replaced by non-negative values (0.01%). Finally, we performed an additive log-ratio (ALR) transformation of relative abundances data using *Cyclicargolithus floridanus* as the denominator, as it is one of the dominant species with continuous occurrences throughout the section. To test the reliability of the PCA outcome, we also performed a classical Q-mode cluster analysis on the same dataset.

3.3. Time-series analysis

Prior to time-series ~~analyses~~analysis, MS series was log-transformed, detrended, linearly interpolated, and resampled at 5 cm (depth-domain) and 6 kyr (age-domain)~~ sampling resolutions~~. ~~Since t~~C~~he MCA Section has available c~~alcium carbonate content ($CaCO_3$)~~ measurements,~~ data with sampling resolution varying between 5 to 11 cm are available~~,~~ from 58 to 72 msl (Savian et al., 2014) and from 108 to 128 msl~~,~~ (Hyland et al., 2009~~; Savian et al., 2014~~).~~,~~ ~~coherence~~ Coherence and phase relationships were calculated between MS and $CaCO_3$ records with the R-package “biwavelet” (Gouhier et al., 2019) based on the MATLAB coherence and phase analysis tool (Grinsted et al., 2004). Spectral analyses, as well as data filtering, were processed in the Acycle software (Li et al., 2019b). Spectral and evolutionary spectral analyses of depth- and age-domain MS series were conducted by applying the multitaper method (MTM) with five 2π prolate tapers (Thomson, 1982) ~~and~~ with conventional AR1 red noise modeling, and ~~with the R-package “astrochron” (Meyers, 2014). Evolutionary wavelet analysis was performed with the R-package “biwavelet” (Gouhier et al., 2019), based on the wavelet program written by Torrence and Compo (1998), and~~the evolutive fast Fourier transform (FFT), respectively~~ analysis was carried out with the Acycle software (Li et al., 2019b)~~. To isolate orbital-linked periodicities, filtered signals were extracted ~~“Astrochron” was also used to extract~~using Gaussian bandpass~~ filters of the MS series,~~ windows~~in order to isolate orbital-linked periodicities~~. The MS filtered signal was manually tuned to the ZB18a astronomical solution (Zeebe and Lourens, 2019) in the QAnalySeries software (Kotov and Pälike, 2018).

4. Results

4.1. Magnetic susceptibility

Magnetic susceptibility measurements indirectly show the concentration and composition of ferromagnetic, diamagnetic, and paramagnetic minerals (Kodama and Hinnov, 2014). These measurements vary between ~0.6 and 22.6 x 10^{-8} m^3/kg, following mainly changes in lithology and increasing towards the top of the section (Fig. 2). Since the section exhibits alternations between marls and limestones, it is hypothesized that MS is inversely proportional to the $CaCO_3$. Therefore, we statistically compare the MS record to published $CaCO_3$ records (Hyland et al., 2009; Savian et al., 2014). Although there is not $CaCO_3$ data throughout the entire section, comparing the MS record with the available $CaCO_3$ records allow us to obtain a reliable response, which covers about half the length of the studied interval, with data at the base and the top of the section. Besides the visual analysis, cross wavelet coherence and phase analysis from the two intervals also demonstrates that MS varies in anti-phase with $CaCO_3$ content (Figs. S1 and S2). Furthermore, we extrapolate this phase relation for the interval without $CaCO_3$ measurements in order to determine the phase relation between MS and eccentricity at the tuning step.

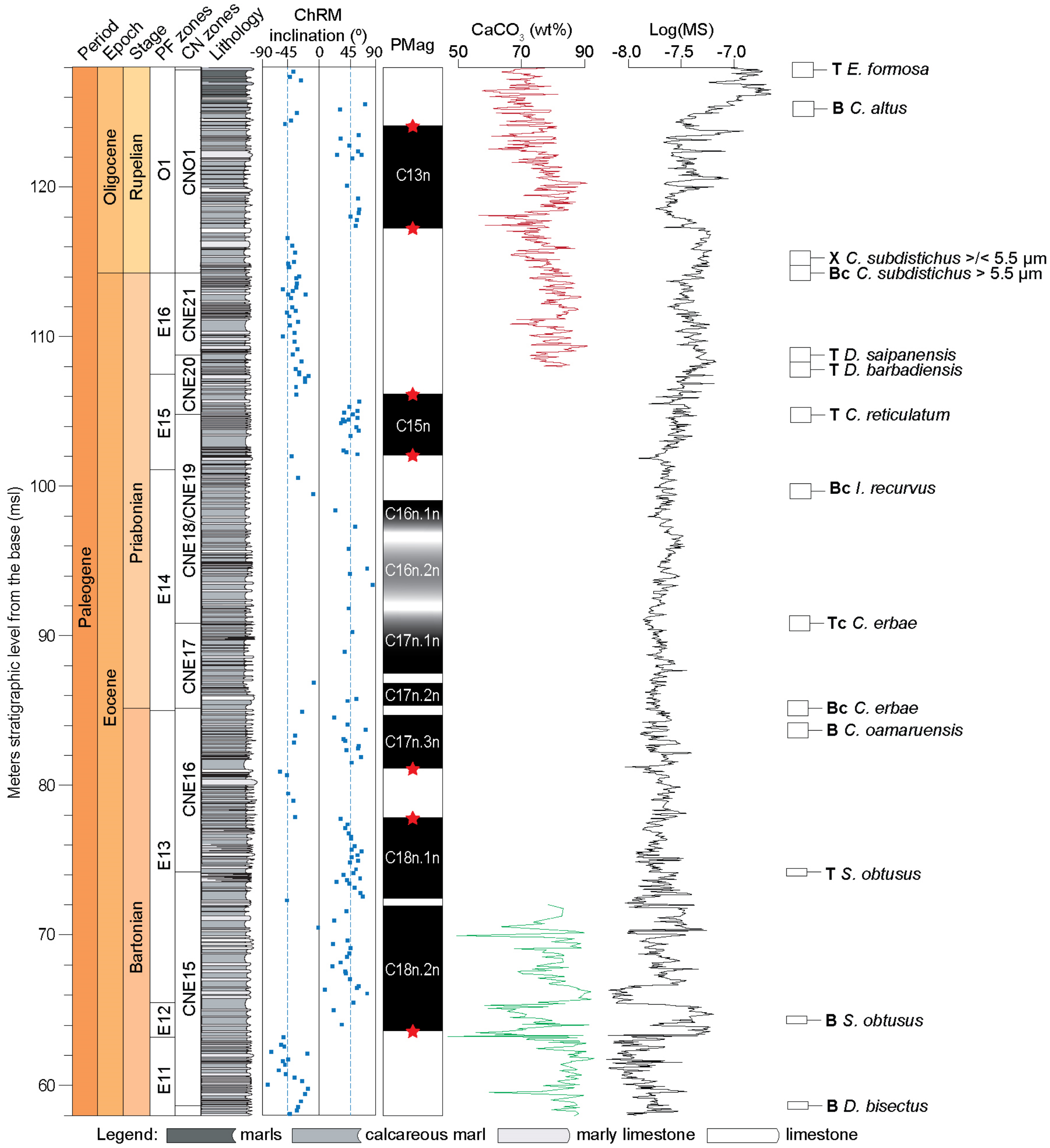

Figure 2. MCA stratigraphic records from 58 to 128 msl spanning the middle Eocene through early Oligocene. From left to right: planktonic foraminifera (PF; Jovane et al., 2013) and calcareous nannofossil (CN; this study) biozonation following the schemes proposed by Wade et al. (2011) and Agnini et al. (2014), lithostratigraphic sequence, characteristic remanent magnetization inclination and magnetostratigraphic interpretation (Jovane et al., 2013), $CaCO_3$ content from Hyland et al. (2009; red) and Savian et al. (2014; green), magnetic susceptibility, and calcareous nannofossil events (this study). The most reliable magnetic polarity reversals are indicated by red stars.

Biostratigraphic uncertainty is represented by unfilled rectangles. B = base; T = top; Bc = base common; Tc = top common; X = crossover.

4.2. Calcareous nannofossil biostratigraphy

Calcareous nannofossils are abundant throughout the section and moderately to poorly preserved. The studied interval spans the Bartonian – early Rupelian, and most of the expected calcareous nannofossil events have been identified. Table 1 summarizes the identified biohorizons and their reliability throughout the studied interval, following the calcareous nannofossil biozonation scheme proposed by Agnini et al. (2014), which provides new events as substitutes for previous standard schemes considered partly unreliable. A detailed description of each datum and the identification of classical biohorizons following the biozonation schemes proposed by Martini (1971) and Okada and Bukry (1980) can be found in the supplementary material.

Depth (m; msl)			Nanno zone boundary	Biostratigraphic datum	Datum confidence
Top	Bottom	Mid-point			
128.00	127.50	127.75	Base CNO2	T *E. formosa*	high
125.50	125.00	125.25		B *C. altus*	high
115.50	115.00	115.25		X *C. subdistichus* >/<5.5 μm	high
114.50	114.00	114.25	Base CNO1	Bc *C. subdistichus* >5.5 μm	high
109.00	108.50	108.75	Base CNE21	T *D. saipanensis*	high
108.00	107.50	107.75		T *D. barbadiensis*	high
105.00	104.50	104.75	Base CNE20	T *C. reticulatum*	high
100.00	99.50	99.75		Bc *I. recurvus*	low
91.00	90.50	90.75	Base CNE18	Tc *C. erbae*	high
85.50	85.00	85.25	Base CNE17	Bc *C. erbae*	high
84.00	83.50	83.75		B *C. oamaruensis*	low
74.25	74.00	74.12	Base CNE16	T *S. obtusus*	high
64.50	64.25	64.37		B *S. obtusus*	high
58.75	58.50	58.62	Base CNE15	B *D. bisectus*	high

Table 1. Calcareous nannofossil biostratigraphic datums for the MCA Section between 58 and 128 msl. B = base; T = top; Bc = base common; Tc = top common; X = crossover.

4.3. Calcareous nannofossil abundance changes and paleoclimatic events

Calcareous nannofossil assemblages show several fluctuations in abundance that were related to environmental variability that characterized the middle Eocene to early Oligocene transition (Fig. 3). Different groups have been recognized in the MCA assemblages. The Coccolithaceae are represented by the genera *Clausicoccus*, *Coccolithus*, *Chiasmolithus* and *Ericsonia*. *Clausicoccus* (mainly small sized) is recorded as scarce (<1%) and discontinuous up to the middle part of the section. From 100 msl up to the section *Clausicoccus* increases in size and abundance. The small sized specimens (<5.5 µm) rapidly increase and show peaks of 5-7%, then they decrease in abundance in proximity of the EOT and are replaced by larger forms of *Clausicoccus* >5.5 to 8 µm. The genus *Coccolithus* consists of *C. pelagicus* and *C. eopelagicus*. The abundance record of the group shows a decreasing trend above the MECO and then a slight increasing trend up to 100 msl. Above this level, *C. pelagicus* becomes one of the major components of the assemblage (about 20%) up to the end of EOT, afterwards a slightly decrease ~~was~~ is observed. The genus *Chiasmolithus* is rare and discontinuously present throughout the section. Few species belonging to this genus are identified, namely *C. grandis*, *C. oamaruensis*, *C. solitus* and *C. altus*. The low percentages (<1%) and the sporadic occurrence prevent here their use as reliable biostratigraphic markers. *Ericsonia formosa* is continuously present with higher abundances (around 10%) in the lower part of the section within the MECO. The overall trend shows a marked decrease from 90 msl up to the top of the section, where the Top of *E. formosa* (127.50 msl) has been observed.

The Noelaerabdaceae are represented by the genera *Cribrocentrum*, *Cyclicargolithus*, *Dictyococcites* and *Reticulofenestra*. *Cribrocentrum* is present from the lower to the middle part of the section, it reaches an acme and then drops in abundance at ~87 msl. This genus, characterized by three marker species *C. reticulatum*, *C. erbae* and *C. isabellae*, shows very pronounced variations in abundance from 1% up to 50% during the acme of *C. erbae*. *Cribrocentrum reticulatum* occurs from the base and gets extinct at 104.75 msl, where it defines the base of CNE20 Zone. *Cribrocentrum erbae* is continuously present from 76 msl, showing a rapid increase in abundance between 85.5 and 91 msl (marker of CNE17 Acme Zone). *Cribrocentrum isabellae* occurs rarely, with very low abundances and seems to be an unreliable bioevent. *Cyclicargolithus floridanus* is among the main calcareous nannofossil constituents of the MCA Section, and shows peaks of abundance (up to 48%) during the MECO. The genus *Dictyococcites* is represented by the two species *D. bisectus* and *D.*

scrippsae. *Dictyococcites bisectus* occurs from the base with percentages around 10%, but very low percentages (<1%) during the MECO have been observed. The abundance of *Dictyococcites scrippsae* vary abruptly (from <1% to 30%) during the MECO interval, but has also wide fluctuations thereafter up to the top of the section. The genus *Reticulofenestra* comprises *R. daviesii*, *R. dictyoda* group (specimens with length >5 and <14 µm and specimens of *R. minutula* <5 µm) and *R. umbilicus* (>14 µm). *Reticulofenestra daviesii* is rare and shows sporadic occurrence in the lower part of the section; it becomes continuous from 92 msl with an increase in abundance around the EOT. Overall, *R. dictyoda* together with *R. umbilicus* show spikes of abundance during the MECO, *R. umbilicus* shows a decreasing trend upwards, while *R. dictyoda* shows an increase in abundance during the EOT.

Discoaster, mainly represented by *D. barbadiensis*, *D. saipanensis* and *D. deflandrei*, exhibits a clear decreasing trend from the lower part of the section upwards that culminates with the extinction (Top) of the *D. barbadiensis* and *D. saipanensis* (rosette-shaped *Discoaster*). A sharp decline of *Discoaster* is noticeable from 84.5 msl. *Discoaster barbadiensis* is commonly more abundant than *D. saipanensis* and shows two peaks in abundance during the MECO. Following the extinctions of the rosette-shaped *Discoaster* at 108 msl, the abrupt decrease in abundance of the whole genus gives rise to a very evident and widespread paracme event, useful for biostratigraphic purpose (Wei and Wise, 1990). *Discoaster* remain below their usual Cenozoic percentages for about 4 Myr, with an abundance of less than 1% in the upper part of the MCA Section. This paracme spans from the top of the NP19-20 to the base of the NP24 (i.e., from C13r to C11n; Maiorano and Monechi, 2006; Tori, 2008).

The genus *Sphenolithus* shows high percentages (roughly 30-40%) during the MECO and post MECO, while upwards a significant decreasing trend has been observed. Several species have been identified: *S. obtusus*, *S. moriformis*, *S. predistentus*, *S. radians*, *S. spiniger* and specimens that can be related to the *S. predistentus-distentus* lineage. The occurrence of *S. furcatolithoides* above its range (CN14 Zone) can be interpreted as reworking or a final tail of distribution as evidenced in several sections (Fornaciari et al., 2010).

Holococcoliths and, in particular, *Lanternithus minutus* and *Zyghrablithus bijugatus* are present throughout the section showing several peculiar changes in abundance. *Lanternithus minutus* occurs throughout the section, is rare during the MECO, shows a slight increase starting from 75.5 to 90 msl, then decreases rapidly above it and significantly rebounds at the top of rosette-shaped *Discoaster*, below the EOT, and through the upper part of the section. *Zygrhablithus bijugatus* is continuously and more or less commonly present, with peaks of abundance in the MECO interval and up to 80 msl; above this level the abundances drop and then increase~~s~~ again below the EOT, with a trend similar to *L. minutus*.

The genus *Helicosphaera* occurs discontinuously in very low percentages (<1%) gathering specimens referable to *H. compacta*, *H. euphratis* and *H. salebrosa*. The same occurs to the calcareous dinoflagellate *Thoracosphaera*, occurring discontinuously throughout the section with percentages <1%.

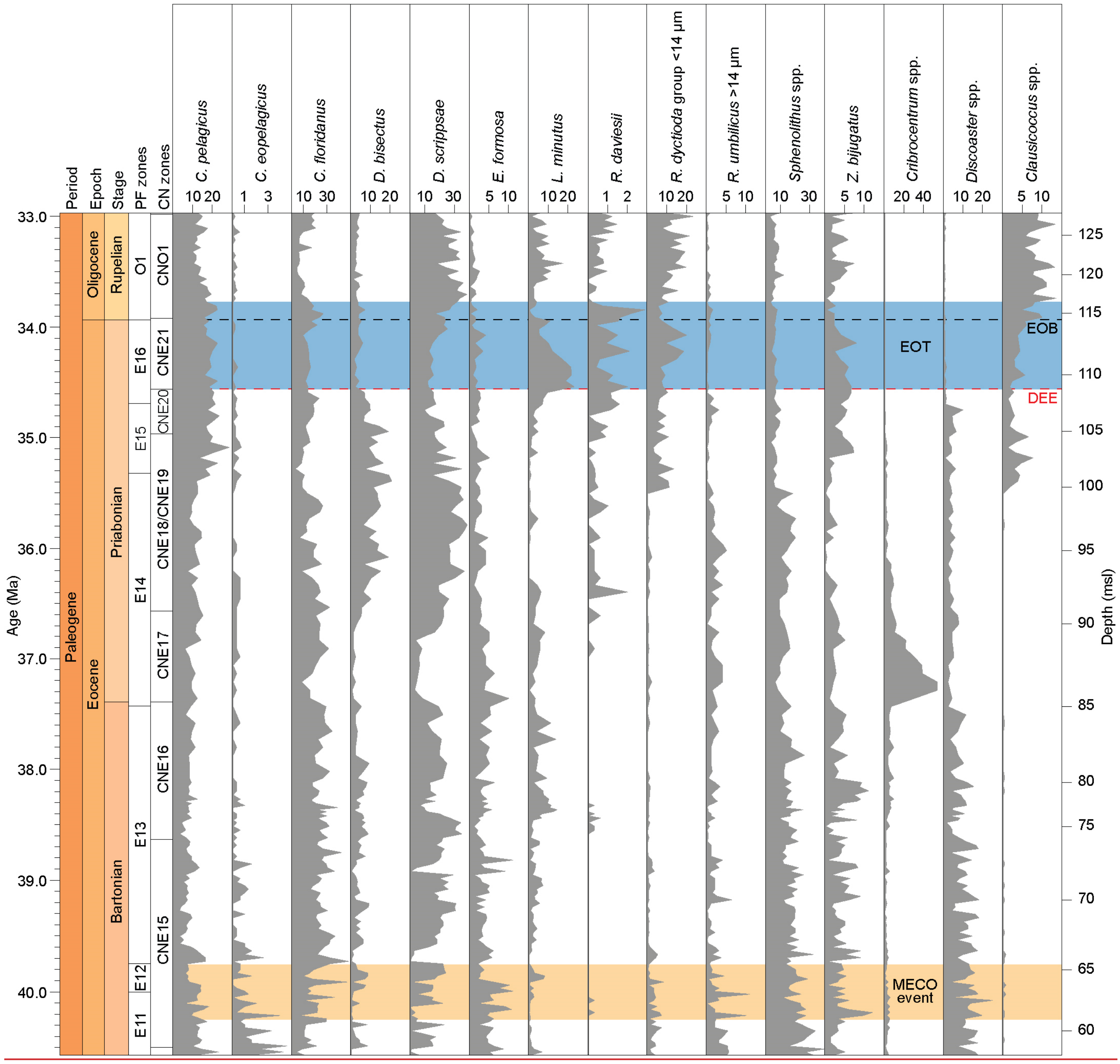

Period
Epoch
Stage
PF zones
CN zones
C. pelagicus
C. eopelagicus
C. floridanus
D. bisectus
D. scrippsae
E. formosa
L. minutus
R. daviesii
R. dyctioda group <14 µm
R. umbilicus >14 µm
Sphenolithus spp.
Z. bijugatus
Cribrocentrum spp.
Discoaster spp.
Clausicoccus spp.
Age (Ma)
Depth (msl)
Paleogene
Oligocene
Eocene
Rupelian
Priabonian
Bartonian
O1
E16
E15
E14
E13
E12
E11
CNO1
CNE21
CNE20
CNE18/CNE19
CNE17
CNE16
CNE15
EOT
EOB
DEE
MECO event

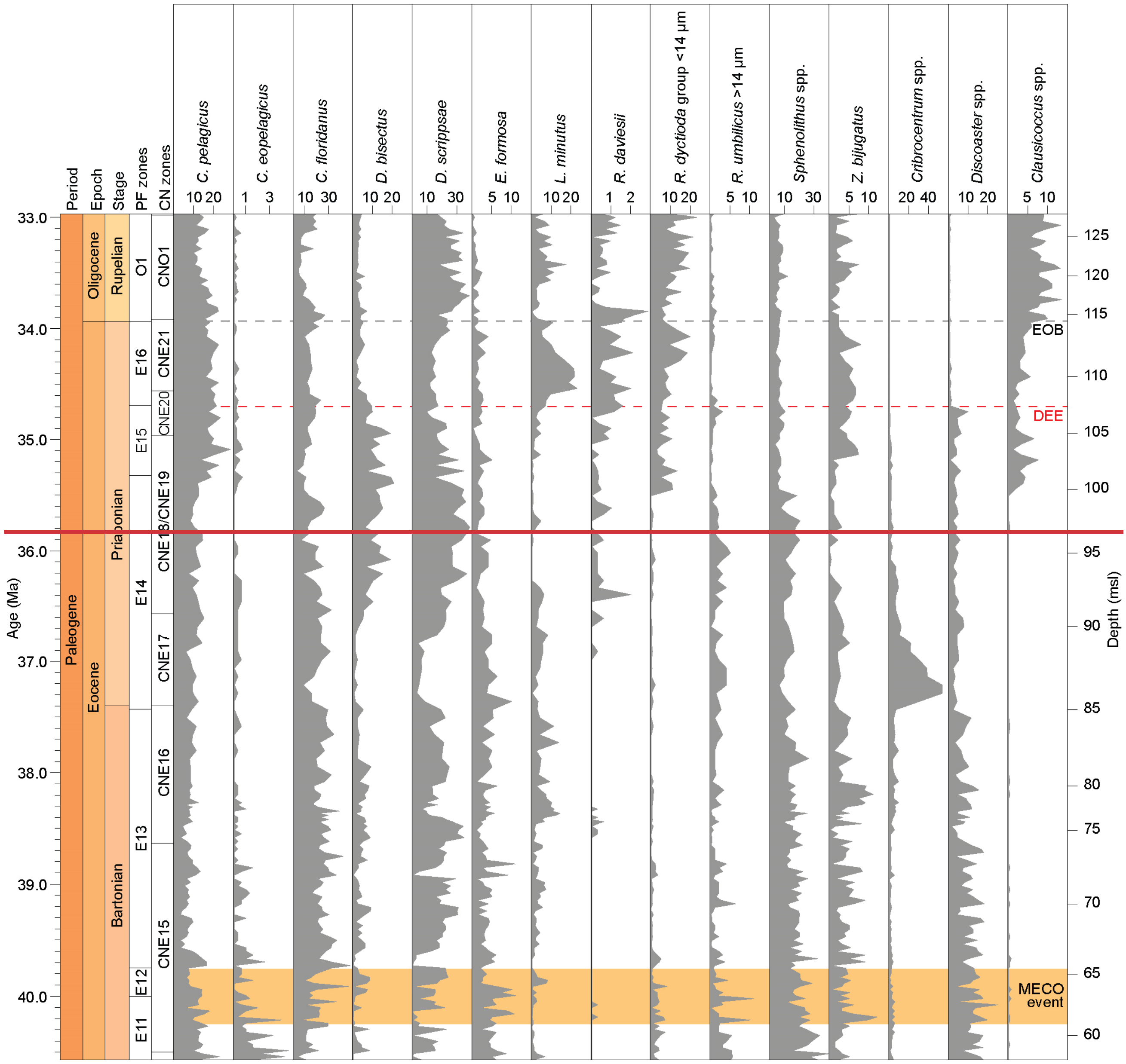

Figure 3. Relative abundance (%) of significant calcareous nannofossil groups and species against orbitally tuned ages. Planktonic foraminiferal (PF; Jovane et al., 2013) and calcareous nannofossil (CN; this study) biozonation following the schemes proposed by Wade et al. (2011) and Agnini et al. (2014), respectively. Black and red horizontal dashed lines indicate the Eocene-Oligocene boundary (EOB) and the *Discoaster* extinction event (DEE), respectively. Blue interval indicates the EOT as a ~790 kyr event started at the extinction of *D. saipanensis* (Hutchinson et al., 2021). ~~The o~~Orange interval indicates the MECO based on its stratigraphic constraint as proposed by Savian et al. (2014).

4.4. Principal component analysis of abundance data

The PCA allows for identifying the hypothetical variables that can explain most of the variance enclosed in the analyzed dataset (Davis, 1986), highlighting groups of samples or taxa which are associated to particular environmental changes. Working in the sample space (with taxa as variables), we have gathered two new matrices, which ~~respectively~~ represent the spatial dispersion of the samples (scores plot and scatter diagram) and the loadings of the taxa on the principal components, respectively (PCs; see Fig. 4). PCs 1 and 2 of the transformed abundance data explain 48.8% and 12.1% of the variance, respectively. A cross-plot and ranked bar charts of PC1 and PC2 loadings display how the calcareous nannofossil taxa define groups of samples (Fig. 4). The PCA scatter diagram displays three clusters that comprise four groups of samples corresponding to different time-intervals (Fig. 4a). The groups are determined by assemblages' variations over time as indicated by the taxa correlations (Fig. 4b) and probably associated to taxa evolutionary turnover and paleoclimatic changes. The recognized clusters are the following: (i) a cluster with negative PC1 is composed of both Bartonian (first group, blue dots) and Priabonian samples (second group, red dots) from the Priabonian/Bartonian boundary up to Bc *I. recurvus*; (ii) a second cluster (third group, pink dots) is composed of Priabonian samples from Bc *I. recurvus* to the *Discoaster* Extinction Event (DEE); (iii) a third cluster (fourth group, green dots) comprises the samples from the DEE to the top of the section. (Fig 4a).

Based on the PCA analysis, we can observe a clear change among the assemblages. Samples from the interval comprising the Bartonian up to the Bc *I. recurvus* show a similar assemblage and are characterized by strong negative PC1 values (mainly characterized by *Cribrocentrum* spp., *Discoaster* spp. and *R. umbilicus*) and variable PC2 values. Thereafter, a "transitional" interval from the Bc *I. recurvus* up to the DEE is associated with changes in the assemblage, with the occurrence of *Clausicoccus, Blackites, R. dictyoda* <14 µm group, *Helicosphaera* + *Pontosphaera* group, and *R. daviesii*, suggesting a cooler and mesotrophic environment. This interval is characterized by increasing PC1 values, ranging from strong negative toward positive values, and also variable PC2 values. Finally, a completely different assemblage has been observed above the DEE characterized by the strongest positive PC1 values and slightly variable PC2 values, suggesting a cooler and eutrophic Oligocene interval (Fig. 4a). Comparable assemblage behavior in PCA analysis has been observed at the DEE event by Jones et al. (2019).

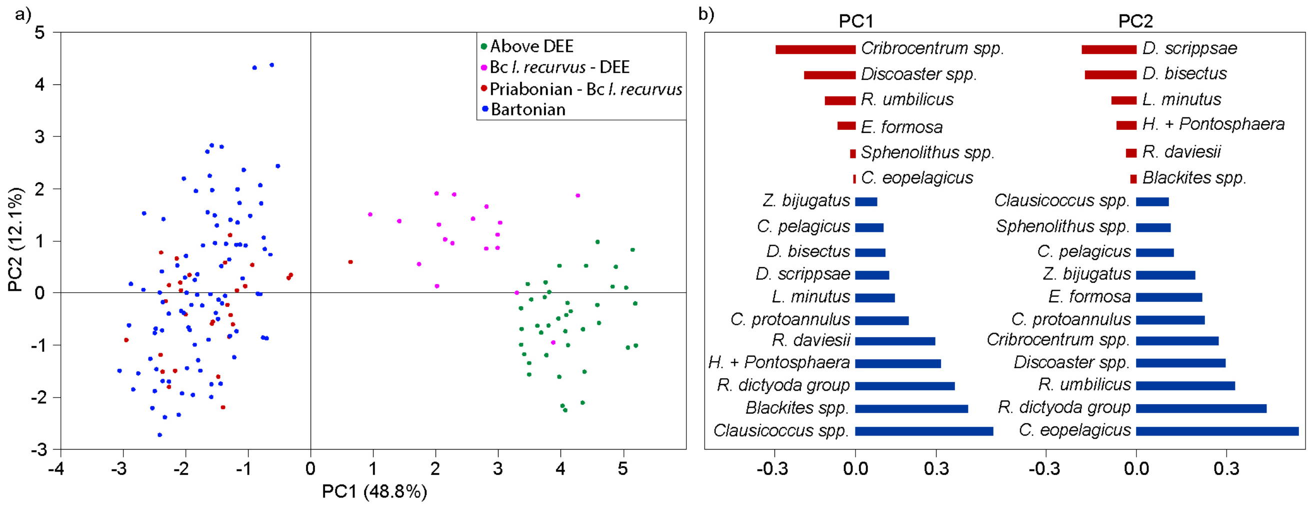

Figure 4. Principal component analysis of the calcareous nannofossil abundance data. a) Cross-plot of PC1 and PC2 showing the four groups of samples. b) Bar charts of PC1 and PC2 loadings showing positive (blue) and negative (red) correlations.

We also performed an alternative PCA analysis on the transposed data matrix (R mode) with the samples as variables, in order to reduce the complexity of the relations among taxa. In this case, PC1 and PC2 explain 60.4% and 17% of the variance, respectively. The PCA scatter diagram shows the dispersion of taxa (scores from PC1 and PC2) and explains the relation between most significant taxa and their paleoecological preferences (Fig. 5). Thus, we can interpret PC1 as a proxy for sea surface temperature, while PC2 probably represents nutrient availability. On this assumption and, in agreement with the literature, *Cribrocentrum* spp., *R. umbilicus* >14 µm, *Discoaster* spp. and *E. formosa* had a preference for a warm and oligotrophic environment (Monechi et al., 2000; Bralower, 2002; Gibbs et al., 2006; Angori et al., 2007; Villa et al., 2008; Schneider et al., 2011; Nyerges et al., 2020), while *C. eopelagicus* and *C. protoannulus* seemed to prefer a cooler and oligotrophic environment (Dunkley Jones et al., 2008). *Reticulofenestra daviesii* had a preference for cold waters regardless of nutrients (Wei and Wise, 1990; Monechi et al., 2000; Villa et al., 2008; 2014; Fioroni et al., 2015) as well as the *Helicosphaera* + *Pontosphaera* group and *Blackites* spp. that were weakly related to nutrients (slightly mesotrophic) and had a preference for cooler environments (Nyerges et al., 2020). *Sphenolithus* had a preference for warm waters (Haq and Lohman, 1976; Wei and Wise, 1990; Aubry, 1992; Wei et al., 1992; Monechi et al., 2000; Bralower, 2002; Tremolada and Bralower, 2004; Villa and Persico, 2006; Schneider et al., 2011) and was, according to our results, weakly related to nutrients, while *Z. bijugatus, L. minutus* and *D. bisectus* were better adapted to warm/temperate waters and also weakly related to nutrient. *L. minutus* and *D. bisectus* seemed slightly mesotrophic adapted. *Dictyococcites scrippsae* and *C. pelagicus* had a preference for warm and eu-mesotrophic waters (Haq and Lohman, 1976; Bukry, 1981; Wei and Wise, 1990); while *Clausicoccus* spp. had a preference for cool and eutrophic waters (Tori, 2008; Nyerges et al., 2020). *Reticulofenestra dictyoda* group <14 µm had a preference for waters rich in nutrients regardless of the temperature (Dunkley Jones et al., 2008; Jones et al., 2019). Therefore, the results of PCA analysis allow us to define paleoenvironmentally significant groups based on the paleoecological preferences of taxa (Table 2). These results are also confirmed by cluster analysis performed on the same dataset (supplementary material; Figs. S3 and S4), where *Z. bijugatus* and *L. minutus* show an additional strict relation, that according to the literature can be related to their preference for near-shore/shelf region (Monechi et al., 2000; Nyerges et al., 2020).

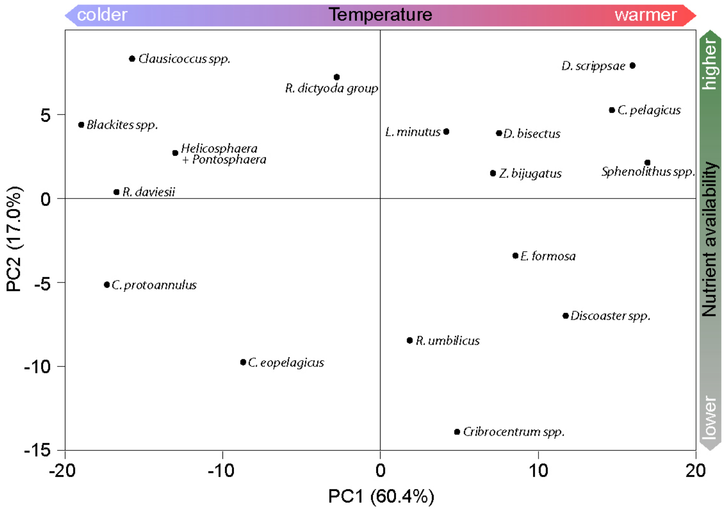

Figure 5. Cross-plot of PC1 and PC2 scores of calcareous nannofossil abundance data and its paleoecological interpretation.

Sea surface water conditions			Trophic conditions	
Warm-water taxa	Warm/Temperate-water taxa	Cool-water taxa	Oligotrophic taxa	Meso-eutrophic taxa
Sphenolithus spp.	*E. formosa*	*Blackites* spp.	*Cribrocentrum* spp.	*Clausicoccus* spp.
D. scrippsae	*D. bisectus*	*C. protoannulus*	*C. eopelagicus*	*D. scrippsae*
C. pelagicus	*Z. bijugatus*	*R. daviesii*	*R. umbilicus* >14 µm	*R. dictyoda group* <14 µm
Discoaster spp.	*Cribrocentrum* spp.	*Clausicoccus* spp.	*Discoaster* spp.	*C. pelagicus*
	L. minutus	*Helicosphaera + Pontosphaera*	*C. protoannulus*	*Blackites* spp.
			E. formosa	*L. minutus*
				D. bisectus

Table 2. Inferred paleoenvironmentally significant groups based on the paleoecological preferences of calcareous nannofossil taxa.

4.5. Orbital tuning

The MCA entire succession consists of rhythmic alternation of calcareous marl and marly limestones with ~~siliciclastic component made up by~~ terrigenous clay and silt (Jovane et al., 2013; Coccioni et al., 2018). Because of the proximity, we adopted here the same interpretation of Jovane et al. (2006, 2010) for the Contessa and Massignano sections that limestone layers (high $CaCO_3$ and low MS) were deposited during cool and dry periods, while marl layers (low $CaCO_3$ and high MS) were deposited during warm and wet periods. Additionally, there is no evidence of large dissolution except during the peak warming within the MECO event in the MCA Section (Savian et al., 2014). Thus, it is reasonable to assume a negative relation between $CaCO_3$ and eccentricity based on the interpretation that high eccentricity enhanced chemical weathering and runoff, which leads to an increase in terrigenous input and, consequently, a relative decrease in the $CaCO_3$ content. Once ~~we have~~ demonstrated that MS reflects mainly $CaCO_3$ variability in an anti-phase relation (Figs. S1 and S2), our adopted strategy was to tune the minima in the long eccentricity filtered MS to the long eccentricity minima from the astronomical solution. The tuning process was constrained by an available $^{206}Pb/^{238}U$ date of 33.291 ± 0.057 Ma for the MCA Section at 123.1 msl (Sahy et al., 2017). Concerning the target curve, despite different astronomical solutions disagree before ~50 Ma due to chaotic behavior of the solar system (e.g., Laskar et al., 2004, 2011a, 2011b; Zeebe, 2017; Zeebe and Lourens, 2019), they all closely agree during the studied interval. We thus opted to use the ZB18a astronomical solution (Zeebe and Lourens, 2019) as the target curve, since it represents the most precise and up to date solution.

To establish a reliable astrochronology, we tuned the MS series to the stable long eccentricity geochronometer, which is related to the Venus-Jupiter ~~resonance~~ interaction (g2-g5) with a period of 405 kyr (Hinnov, 2018). Magnetostratigraphic interpretation from Jovane et al. (2013) gives a mean SAR of 0.86 cm kyr^{-1} for the studied interval. Based on this SAR, we can assume that the stable long eccentricity cycle (405 kyr) has a mean thickness of ~3.5 m. MTM spectrum and ~~wavelet analysis~~evolutive FFT of the MS series in the stratigraphic domain corroborates this assumption and displays a stable and strong signal around this periodicity (Fig. 6 ~~and S5~~). The MTM analysis shows two distinct peaks within the interpreted long eccentricity bandwidth, at 0.19 and 0.30 cycles m^{-1}, corresponding to periodicities of ~5.2 and ~3.3 m (Fig. 6). Using a Gaussian bandpass filter centered at the average frequency between those peaks~~With a Gaussian bandpass filter~~ (0.25 cycles m^{-1})~~,~~ we extracted the ~~long~~ 405 kyr eccentricity signal from the MS series and tuned it to the long eccentricity signal from the ZB18a astronomical solution (Fig. 7). It is noteworthy that the evolutive FFT shows a drastic shift in the long eccentricity signal towards a lower frequency in the interval between ~75 to

~80 msl (Fig. 6), implying an increased SAR within this interval. Although abrupt, this higher SAR interval was already identified in the bio- and magnetostratigraphic age model from Jovane et al. (2013). Once interpreting this interval as two long eccentricities cycles would result in an interval with lower SAR compared to the surrounding interval, it was interpreted as a single long eccentricity cycle (Fig. 7).

434

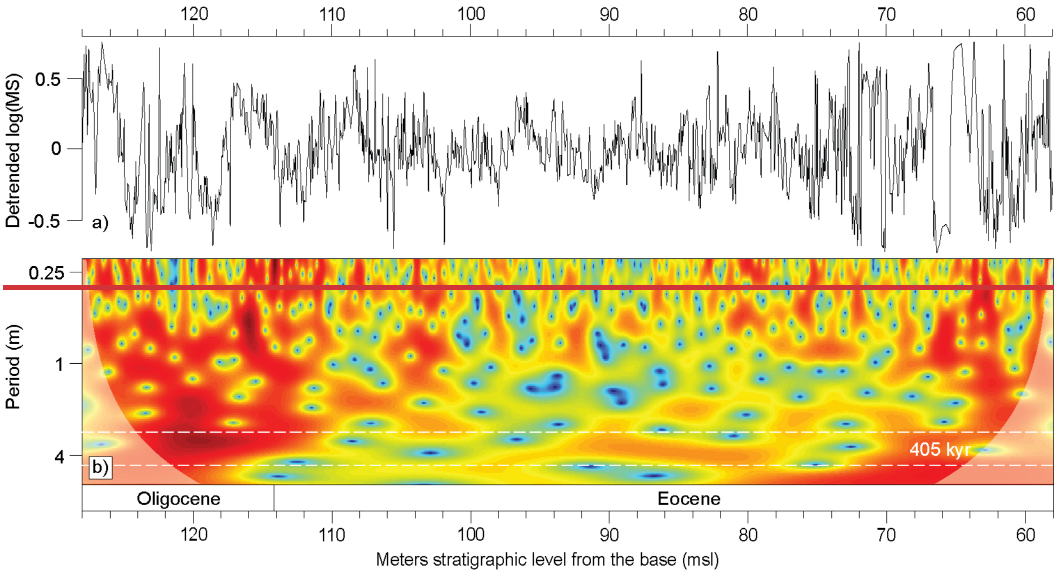
120
110
100
90
80
70
60
Detrended log(MS)
0.5
0
-0.5
a)
0.25
Period (m)
1
4
b)
405 kyr
Oligocene
Eocene
Meters stratigraphic level from the base (msl)

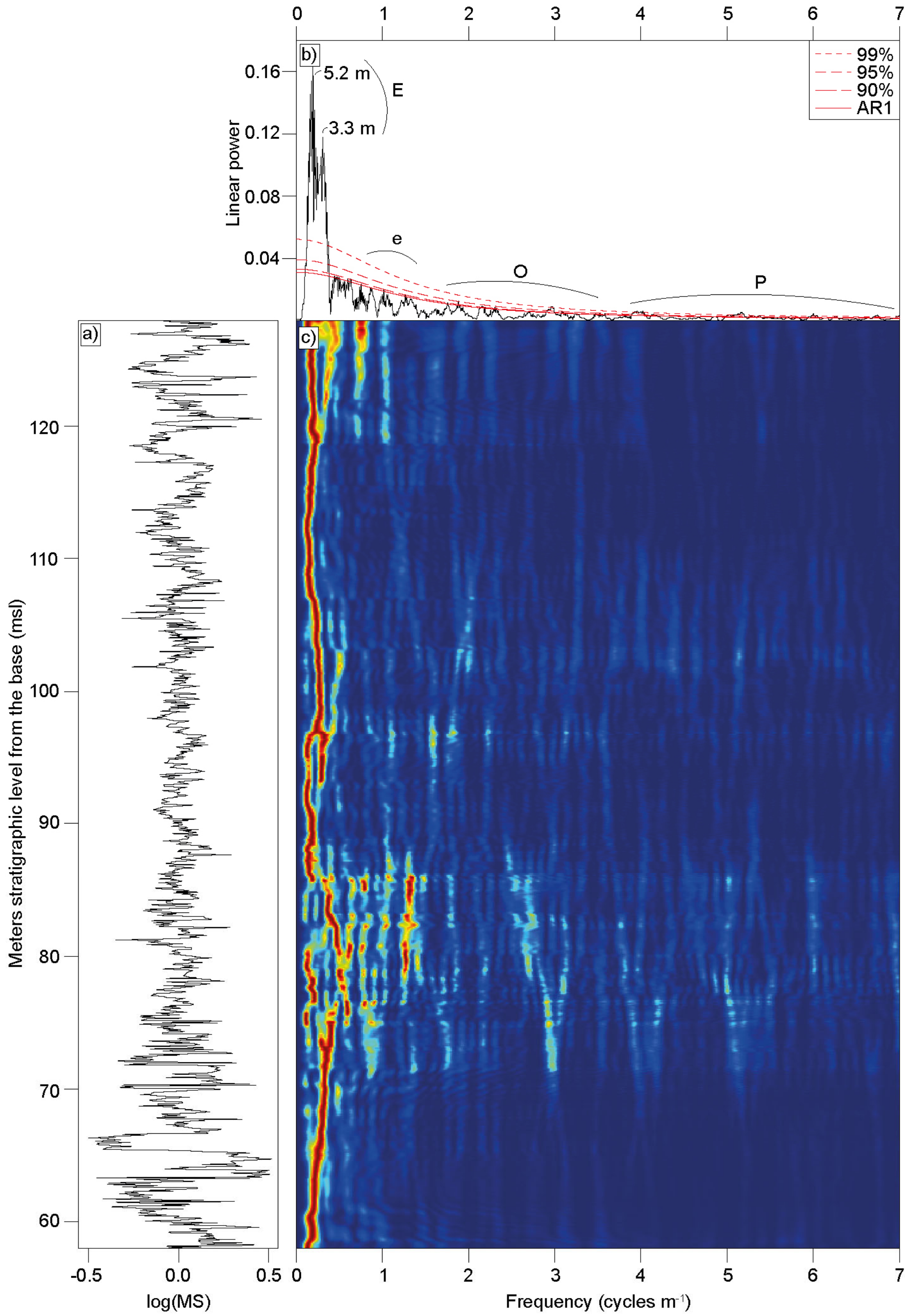

Figure 6. Spectral analysis of the MS series in the stratigraphic domain. a) Log-transformed, detrended and 5-cm interpolated MS series with low-frequency noise removed after high-pass filtering (cut frequency of 0.1 cycles m^{-1}). b) MTM power spectrum and estimated noise spectrum and confidence levels. Interpreted long-, and short-eccentricity, obliquity, and precession bandwidths are labeled as E, e, O, and P, respectively. Orbital cycles were interpreted based on the bio- and magnetostratigraphic age model from Jovane et al. (2013). c) Evolutive FFT with a 10 m sliding window.~~Evolutionary wavelet analysis of the MS series with the 405 kyr long eccentricity~~

~~interpreted based on the magnetostratigraphic SAR of 0.86 cm kyr^{-1} (Jovane et al., 2013). Warm colors indicate high spectral power, and the white shaded areas represent the "cone of influence", where edge effects become important (Grinsted et al., 2004).~~

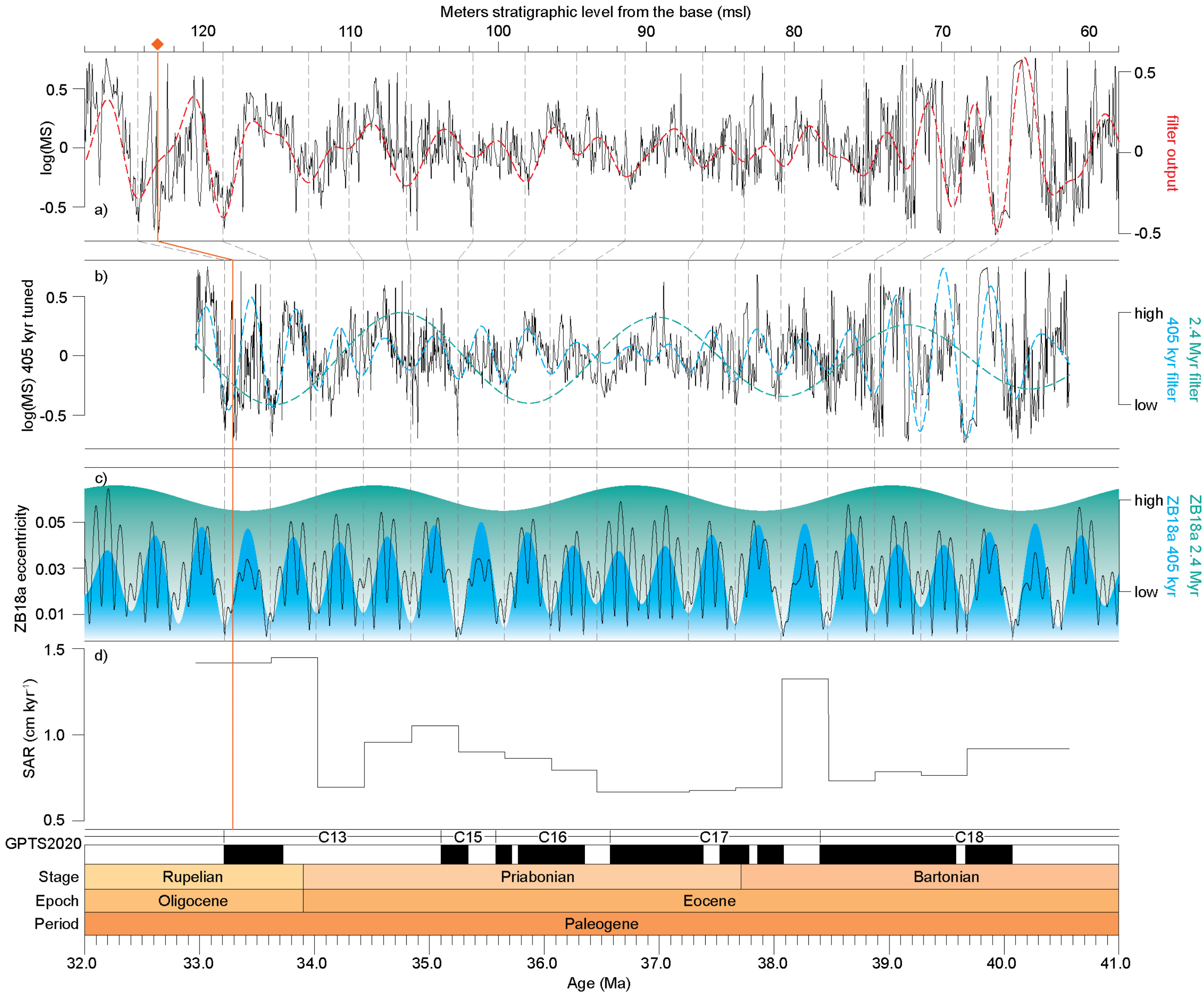

Meters stratigraphic level from the base (msl)
120
110
100
90
80
70
60
log(MS)
filter output
a)
b)
log(MS) 405 kyr tuned
high
low
2.4 Myr filter
405 kyr filter
c)
ZB18a eccentricity
ZB18a 2.4 Myr
ZB18a 405 kyr
d)
SAR (cm kyr⁻¹)
GPTS2020
C13
C15
C16
C17
C18
Stage
Rupelian
Priabonian
Bartonian
Epoch
Oligocene
Eocene
Period
Paleogene
32.0
33.0
34.0
35.0
36.0
37.0
38.0
39.0
40.0
41.0
Age (Ma)

447

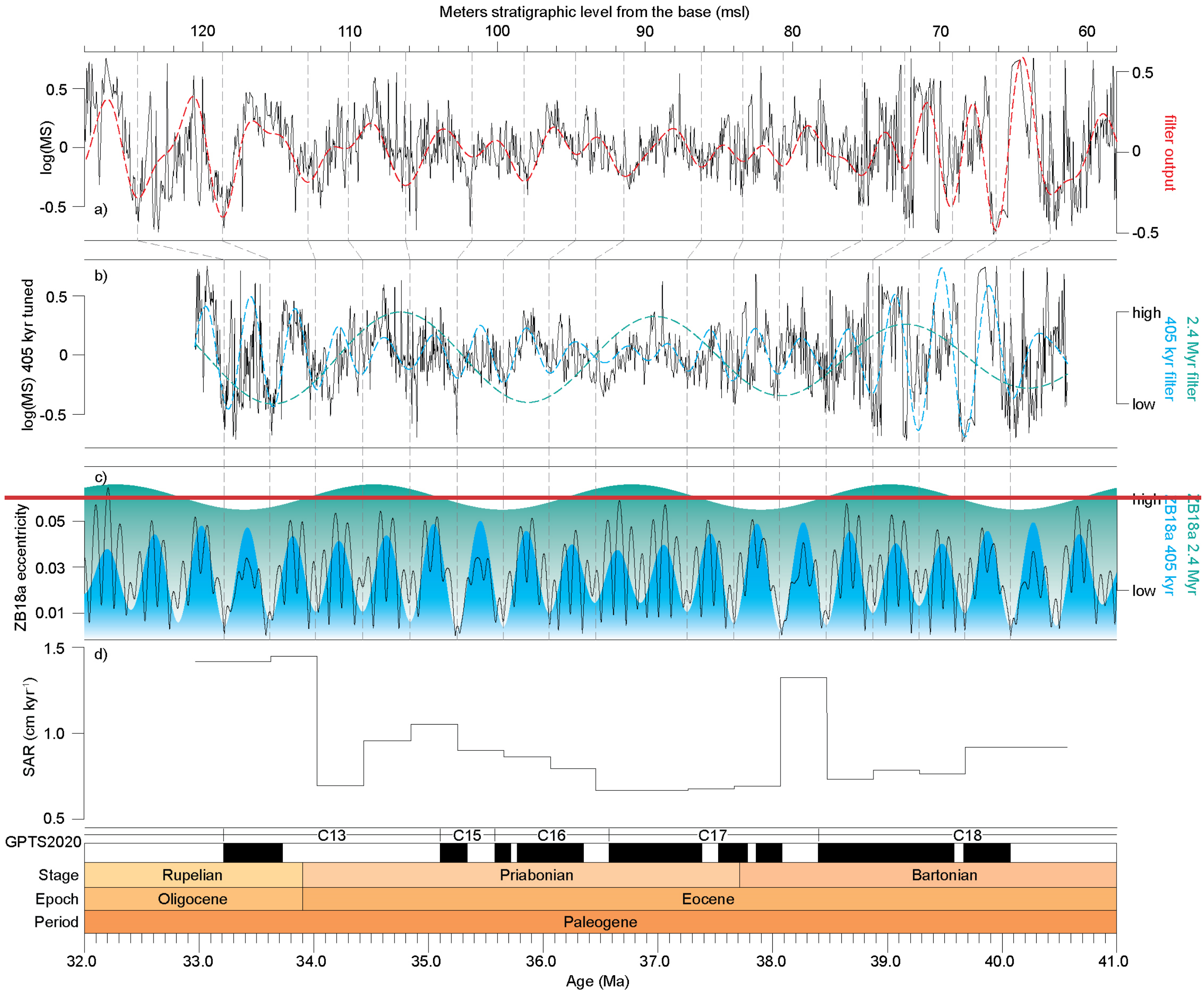

Figure 7. Astronomical calibration of the MCA Section. a) MS record in the stratigraphic domain and the interpreted 405 kyr cycle extracted with a Gaussian bandpass filter centered at 0.25 ± 0.13 cm^{-1} (red dashed line). b) Long-eccentricity tuned MS record with the 405 kyr (blue dashed line) and the 2.4 Myr (green dashed line) components filter outputs. c) ZB18a astronomical solution (Zeebe and Lourens, 2019) with the 405 kyr (blue area) and the 2.4 Myr (green area) components. d) Tuning-derived sediment accumulation rate (SAR). Orange diamond and line represent the ^{206}Pb/^{238}U radioisotope age tie point (Sahy et al., 2017). Vertical gray dashed lines show the tuning tie points. The 405 kyr and the 2.4 Myr components were extracted with a Gaussian bandpass filter centered at 0.002469 ± 0.0006 kyr^{-1}, and 0.00042 ± 0.00004 kyr^{-1} respectively. Polarity time scale is from GPTS 2020 (Ogg, 2020). Period, Epoch, and Stage from GTS2020 (Speijer et al., 2020).

Furthermore, we intended to perform a fine-tuning at the short eccentricity level, but due to a weak short eccentricity signal in the MS series, even after the 405 kyr tuned (Fig. 8), we opted to use only the long eccentricity tuning in order to maintain the robustness of the MCA age model. This weak signal is probably due to the fact that MS reflects mainly $CaCO_3$, which in some Neo-Tethys sections, such as the Alano Section, show a weak short eccentricity signal (Galeotti et al., 2019). Galeotti et al. (2019) suggested the sum of changes in runoff and tectonic activity (Doglioni and Bosellini, 1987; Carminati and Doglioni, 2012) as a possible cause. Another possible cause is related to the low SAR leading to a smoothing in the precession signal ~~and this~~which, in turn, would have obliterated the eccentricity signal, as shown at Blake Nose (Röhl et al., 2001, 2003) and Walvis Ridge sites (Lourens et al., 2005; Westerhold et al., 2007), in the Atlantic Ocean. We thus suggest a future astrochronological refinement study for the MCA using a different proxy in order to resolve the short eccentricity signal, such as carbon isotope records, which seem~~s~~ to better resolve this cycle (e.g., Galeotti et al., 2019; Giorgioni et al., 2019). Despite of it, spectral analysis of the resultant ~~400~~ 405 kyr orbitally tuned MS series displays strong signals in orbital frequencies of long eccentricity, obliquity, and precession (Fig. 8), suggesting that our orbital tuning is reliable. Another important feature to support its robustness is that our estimated age based solely on the tuning process for 123.1 msl is 33.304 Ma, a difference of only 13 kyr to the available high-resolution radiometric date for the same stratigraphic level (Sahy et al., 2017). The presence of a precessional signal suggests that the absence of a reliable signal within the short eccentricity band is most likely explained by the first of the two mentioned hypotheses. It is also worth noting the presence of a prominent obliquity signal in the power spectrum (Fig. 8a), despite the relatively low latitude of the MCA Section. The evolutive FFT analysis shows that the obliquity seems to exert more influence on the MS record mainly near the EOT interval (Fig. 8b), an orbital configuration similar to those identified by Galeotti et al. (2016) in high latitudes, and recently by Messaoud et al. (2020) in another Neo-Tethys section. The reliability of our age model is also corroborated by the matching between the 2.4 Myr amplitude modulation component of the resultant tuned MS series with the one from the astronomical solution

(Fig. 7). Furthermore, the SAR derived from the independent orbital tuning (Fig. 7d) agrees with the first lower resolution SAR curve derived from the magnetostratigraphy (Jovane et al., 2013).

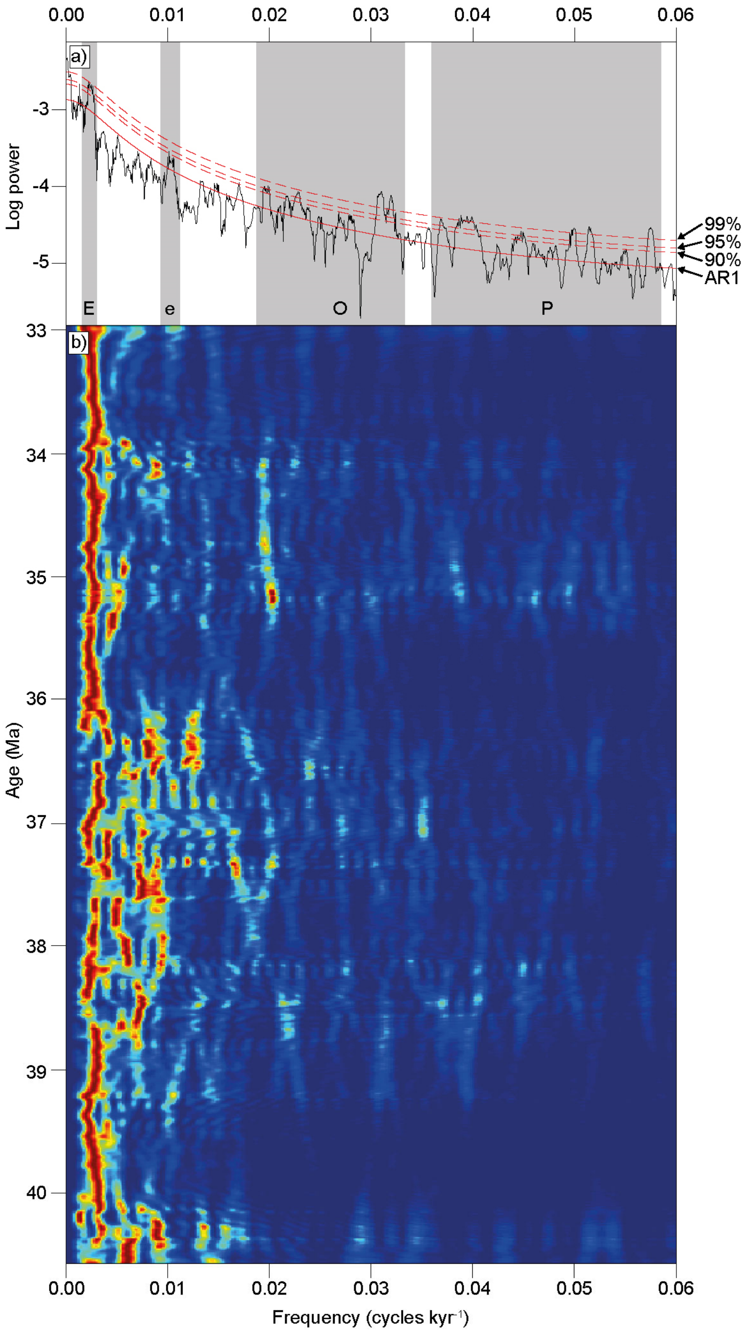

Figure 8. Power spectra of MS record on astrochronology. a) MTM power spectrum and estimated noise spectrum and confidence levels. Long- and short-eccentricity, obliquity, and precession bandwidths are shown by gray areas labeled as E, e, O, and P, respectively. b) Evolutive FFT with an 800 kyr sliding window.

5. Discussion

The developed astrochronologic time scale allows us to revise the previous MCA chronologic framework based on magnetostratigraphy (Jovane et al., 2013) and better constrain important events recorded within the section, such as the MECO, the EOT, and the Oi-1 event. Our long eccentricity tuning, together with new high-resolution calcareous nannofossil biostratigraphy, suggest that the MCA Section is complete, at least at the scale of hundreds of thousands of years.

5.1. Comparison of MCA chron positions and durations

Based on the most up to date magnetostratigraphic interpretation for the MCA (Jovane et al., 2013), together with our developed astrochronologic age model, new ~~magnetochrons~~ polarity chrons boundaries ages and durations between chrons C18n and C13n have been estimated and compared to standard and tuning-derived magnetic polarity reversals ages for the same interval (Tables 3 and 4). Firstly, we ~~point out~~highlight the similarity between our estimated ages with the ones from Hyland et al. (2009) for the common time intervals. This fact corroborates both~~,~~ the consistency of the MCA astrochronology, at least in the upper part of the section, and once again that MS represents mainly changes in $CaCO_3$ content. On the other hand, due to ambiguous data from magnetostratigraphy (Fig. 2), there are ages and durations discrepancies in the lowest part, and also unidentified reversals in the middle part of the section, which require a refined magnetostratigraphic analysis in order to solve this issue (Tables 3 and 4). Despite these discrepancies, the reliable magnetostratigraphic data in the lowest part of the section allow us to estimate the age of the onset of ~~magnetochron~~ Chron C18n based on astrochronology. The onset age of ~~magnetochron~~ Chron C18n is relatively younger when compared to classical standards and tuning-derived ages, but it coincides surprisingly well with the age proposed by ~~the recent middle Eocene astronomical timescale from~~ Boulila et al. (2018; Table 3), even though the geological record studied has a controversial stratigraphic interpretation (Vahlenkamp et al., 2020). Despite that, once ~~Since it~~this reversal is positioned within the MECO interval, ~~this reversal age~~it is ~~also~~ important to support our further time constraint of the event in the MCA Section.

Chron	Standard GPTS				Astronomically calibrated							
	CK95 (Cande and Kent, 1995)	GPTS 2004 (Ogg and Smith, 2004)	GPTS 2012 (Ogg, 2012)	MQSD20 (Malinverno et al., 2020)	ODP Site 1218 (Pälike et al., 2006)	Massignano (Jovane et al., 2006)	Monte Cagnero (Hyland et al., 2009)	Contessa Highway (Jovane et al., 2010)	PEAT Sites (Westerhold et al., 2014)	IODP Exp. 342 composite U1408-U1410 (Boulila et al., 2018)	Monte Cagnero (this study[a])
C13n (y)	33.058	33.266	33.157	33.076	33.232		33.230		33.214		**33.231**
C13n (o)	33.545	33.738	33.705	33.675	33.705		33.750		33.726		**33.712**
C15n (y)	34.655	34.782	34.999	34.875	35.126	34.640			35.102		**34.836**
C15n (o)	34.940	35.043	35.294	35.199	35.254	34.960			35.336		**35.202**
C16n.1n (y)	35.343	35.404	35.706	35.627	35.328	35.343			35.580		35.540
C16n.1n (o)	35.526	35.567	35.892	35.863	35.554				35.718		-
C16n.2n (y)	35.685	35.707	36.051	36.054	35.643				35.774		-
C16n.2n (o)	36.341	36.276	36.700	36.728	36.355				36.351		-
C17n.1n (y)	36.618	36.512	36.969	37.049	36.668				36.573		-
C17n.1n (o)	37.473	37.235	37.753	37.741	37.520				37.385		36.982
C17n.2n (y)	37.604	37.345	37.872	37.934	37.656				37.530		37.220
C17n.2n (o)	37.848	37.549	38.093	38.150	37.907				37.781		37.372
C17n.3n (y)	37.920	37.610	38.159	38.287	37.956				37.858		37.439
C17n.3n (o)	38.113	37.771	38.333	38.477	38.159				38.081		**37.973**
C18n.1n (y)	38.426	38.032	38.615	38.835	38.449				38.398	38.527	**38.273**
C18n.1n (o)	39.552	38.975	39.627	39.734	39.554				39.582	39.458	38.861
C18n.2n (y)	39.631	39.041	39.698	39.897	39.602				39.666	39.597	38.929
C18n.2n (o)	40.130	39.464	40.145	40.366	40.084			40.120	40.073	39.989	**39.959**

[a] Tuned to the ZB18a astronomical solution (Zeebe and Lourens, 2019).

Table 3. Comparison of ~~magnetochron~~polarity chron-~~-~~ boundary ages in millions of years (Ma). In our estimated ages column, bold numbers represent the most reliable magnetostratigraphic interpretation, whereas regular font numbers represent ambiguous interpretation and hyphen represents the boundaries that were not identified. For the studied interval, the recently published GPTS 2020 (Ogg, 2020) used all ages from the Pacific Equatorial Age Transect (PEAT) sites (Westerhold et al., 2014).

Chron	Standard GPTS				Astronomically calibrated					
	CK95 (Cande and Kent, 1995)	GPTS 2004 (Ogg and Smith, 2004)	GPTS 2012 (Ogg, 2012)	MQSD20 (Malinverno et al., 2020)	ODP Site 1218 (Pälike et al., 2006)	Massignano (Jovane et al., 2006)	Monte Cagnero (Hyland et al., 2009)	PEAT Sites (Westerhold et al., 2014)	IODP Exp. 342 composite U1408-U1410 (Boulila et al., 2018)	Monte Cagnero (this study[a])
C13n	0.487	0.472	0.548	0.599	0.473		0.520	0.512		**0.481**
C13r	1.110	1.044	1.294	1.200	1.421			1.376		**1.124**
C15n	0.285	0.261	0.295	0.324	0.128	0.320		0.234		**0.366**
C15r	0.403	0.361	0.412	0.428	0.074	0.383		0.244		0.338
C16n.1n	0.183	0.163	0.186	0.236	0.226			0.138		-
C16n.1r	0.159	0.140	0.159	0.191	0.089			0.056		-
C16n.2n	0.656	0.569	0.649	0.674	0.712			0.577		-
C16n.2r	0.277	0.236	0.269	0.321	0.313			0.222		-
C17n.1n	0.855	0.723	0.784	0.692	0.852			0.812		-
C17n.1r	0.131	0.110	0.119	0.193	0.136			0.145		0.238
C17n.2n	0.244	0.204	0.221	0.216	0.251			0.251		0.152
C17n.2r	0.072	0.061	0.066	0.137	0.049			0.077		0.067

C17n.3n	0.193	0.161	0.174	0.190	0.203	0.223		0.534
C17n.3r	0.313	0.261	0.282	0.358	0.290	0.317		**0.300**
C18n.1n	1.126	0.943	1.012	0.899	1.105	1.184	0.931	0.588
C18n.1r	0.079	0.066	0.071	0.163	0.048	0.084	0.139	0.068
C18n.2n	0.499	0.423	0.447	0.469	0.482	0.407	0.392	1.030

[a] Tuned to the ZB18a astronomical solution (Zeebe and Lourens, 2019).

Table 4. Comparison of ~~magnetochron~~ polarity chron boundary durations in millions of years (Myr). In our estimated durations column, bold numbers represent reliable magnetostratigraphic interpretation for base and top boundaries, whereas regular font numbers represent ambiguous interpretation for either base and/or top boundaries, and hyphen represents that base and/or top boundaries were not identified. For the studied interval, the recently published GPTS 2020 (Ogg, 2020) used all ages from the PEAT sites (Westerhold et al., 2014), resulting in the same durations.

5.2. MCA biostratigraphy

Integrating the planktonic foraminiferal (Jovane et al., 2013) and our revised calcareous nannofossil biostratigraphies, together with the developed age model, we provide here an ~~up to date~~up-to-date biostratigraphic framework for the MCA Section spanning the middle Eocene to the early Oligocene interval. Jovane et al. (2013) identified all planktonic zones proposed by Wade et al. (2011) for the same interval of our study, which spans zones E11 through O1. Revisiting the calcareous nannofossil biostratigraphy and following the biozonation from Agnini et al. (2014), we were able to define all the biozones that characterize the studied interval (CNE15 to CNO2), except for the base of CNE19, defined by the base of *C. isabellae*. Based on our developed orbitally tuned age model, we have been able to place the important calcareous nannofossil and planktonic foraminiferal biohorizons identified in the MCA Section on a timeframe and compare our estimated ages with those of Agnini et al. (2014) and Wade et al. (2011) (Table 5).

Our estimated planktonic foraminiferal ages based on the biostratigraphy from Jovane et al. (2013) are in agreement with those proposed by Wade et al. (2011). Differences are around 200 kyr, except for the base of zone E15 with a relatively higher offset (Table 5). It is noteworthy the similarity between the proposed and our estimated age for the extinction of *H. alabamensis*, marker for the EOB (Premoli Silva and Jenkyns, 1993). The calculated age of the EOB does not only match recent ones (e.g., Speijer et al., 2020) but is also virtually the same age – less than 20 kyr of difference – found by Hyland et al. (2009) in their MCA study, once again ~~pointing out~~highlighting the robustness of MCA astrochronology.

Estimated ages for calcareous nannofossil markers seem to agree even better than planktonic foraminifera, which may result from the higher sampling resolution. Most of the estimated ages closely agrees to those of Agnini et al. (2014) with less than ~150 kyr of difference (Table 5). This is particularly true for zones CNO1 and CNO2 that display offsets of 40 and 60 kyr, respectively, which once again support our estimated age for the EOB. The exceptions are the bases of zones CNE17, CNE18, and CNE20, which have differences of approximately 500, 900, and 300 kyr, respectively. Despite the relatively high age difference, we suggest the base of common *C. erbae* as the most reliable datum in the MCA Section for the base of the Priabonian stage, since its GSSP was recently ratified (Agnini et al., 2020) as the base of the Tiziano bed in the Alano Section with an astrochronological age of 37.710±0.01 Ma (Galeotti et al., 2019).

Zone (base)	Biostratigraphic datum	Age (Ma)		
		CN zones (Agnini et al., 2014)	**PF zones (Wade et al., 2011)**	**Monte Cagnero (this study)**
CNO2	T *E. formosa*	32.92		32.98
CNO1	Bc *C. subdistichus* >5.5 µm	33.88		33.92
O1	T *H. alabamensis*		33.9	33.93
CNE21	T *D. saipanensis*	34.44		34.56
E16	T *G. index*		34.5	34.69
CNE20	T *C. reticulatum*	35.24		34.96
E15	T *G. semiinvoluta*		35.8	35.32
CNE18	Tc *C. erbae*	37.46		36.57
CNE17	Bc *C. erbae*	37.88		37.39
E14	T *M. crassatus*		37.7	37.43
CNE16	T *S. obtusus*	38.47		38.63
E13	T *O. beckmanni*		39.4	39.75
E12	B *O. beckmanni*		39.8	40.00
CNE15	B *D. bisectus*	40.34		40.50

Table 5. Estimated ages for calcareous nannofossil (CN) and planktonic foraminiferal (PF) zones compared to their respective standard ages. CN and PF biozonations are after Agnini et al. (2014) and Wade et al. (2011), respectively.

5.3. Paleoenvironmental and paleoclimatic implications

Increasing sedimentation rates towards the top of the section (Fig. 7) (Jovane et al., 2013 and this study) agrees with paleobathymetric estimates by benthic foraminiferal data (Guerrera et al., 1988; Parisi et al., 1988), which ~~points out to~~indicate a gradual shallowing from lower bathyal (1000-2000 m) during the middle Eocene to upper bathyal depth (400-600 m) in the early Oligocene. This could explain a relative increase in SAR simply by increasing the terrigenous input due to the gradually more proximal sediment input setting. Following the interpretation that MS reflects mostly terrigenous input in a pelagic carbonate succession, a sea level fall would lead to an increase in the terrigenous/carbonate ratio, which can be observed in the raw MS data by its gradually increasing values towards the top of the MCA Section (Fig. 2).

The MCA Section is one of the few middle latitude successions that records continuous, rich, and well preserved calcareous nannoflora, enabling the reconstruction of the biotic and paleoceanographic changes from middle Eocene to lower Oligocene. We can observe significant changes in the calcareous nannofossil assemblages within the studied interval (Fig. 3). Modifications in the abundances of calcareous nannofossil taxa are mainly related to paleoenvironmental changes. Paleotemperatures and paleofertility are the main factors that affect the presence and abundance of taxa. Up to now, it does not exist a specific scheme that establishes the paleoecological preferences of calcareous nannofossils, because species preferences could have changed through time and among different biogeographical settings. However, a general agreement on the preferences of some taxa can be identified. To infer possible temperature and trophic variations of surface waters, most calcareous nannofossils were allocated into groups of environmental affinities, largely following Haq and Lohmann (1976), Aubry (1992), Gardin and Monechi (1998), Monechi et al. (2000), Bralower (2002), Persico and Villa (2004), Tremolada and Bralower (2004), Gibbs et al. (2006), Villa et al. (2008, 2014), Agnini et al. (2011), Jones et al. (2019) and Nyerges et al. (2020). Together with the cited literature, the multivariate statistical analysis performed on the MCA calcareous nannofossil dataset allowed the recognition of major community changes and the identification of five groups of taxa with similar paleoecological preferences as shown in Figure 9 and Table 2.

Variations in relative abundances of the paleoenvironmentally significant groups revealed important environmental changes and trends throughout the MCA Section (Fig. 9). Overall, we can observe that the warm and warm/temperate-water taxa are quite abundant throughout the section with a slightly decreasing trend in the upper part of the section. Cool-water taxa ~~were~~ are rare until the upper Priabonian at ~35.5 Ma (100 msl) coinciding with the base of the range of *I. recurvus* and an enrichment in meso-eutrophic taxa. These taxa increased in abundance during the EOT, corroborating the long-term global cooling. A peak in abundance of oligotrophic taxa is observed in the early Priabonian at ~37.3 Ma (86 msl) related to the acme of *C. erbae* (marker of the CNE7 zone). Despite that, oligotrophic taxa show a decreasing trend with an abrupt drop in abundance and diversity related to the extinction of the rosette-shaped *Discoasters*, which has been recently defined as the *Discoaster* Extinction Event (DEE; Jones et al., 2019). Jones et al. (2019) placed the event between 34.44 and 34.77 Ma, while a recent study in the southwestern Neo-Tethys estimated an orbitally tuned age of 34.35 Ma for the event (Messaoud et al., 2020). Based on our orbitally tuned age model, the extinctions of *D. saipanensis* and *D. barbadiensis* occurred respectively at 34.58 and 34.69 Ma (Fig. 3), therefore agreeing better with the estimated ages from Jones et al. (2019). On the contrary, meso-eutrophic taxa increased in abundance starting at ~37.0 Ma (89 msl), defining ~~an abundance reversal or~~ a definitive crossover from oligotrophic to mesotrophic taxa dominance.

In the lower part of the section (up to the acme of the *Cribrocentrum*), several fluctuations in abundance between oligotrophic and mesotrophic taxa have been observed with a persistent dominance of warm-water taxa. ~~Despite~~ Although the MECO event could be defined as a warm oligotrophic interval, it still shows very dynamic cycles (Giorgioni et al., 2019). At the onset of the MECO event, a reduction of *D. bisectus* and *Sphenolithus* (oligotrophic taxa) was associated with a sharp increase in the abundance of *C. floridanus* (eutrophic taxon), *Z. bijugatus*, and small *Reticulofenestra* (Fig. 3). The MECO interval is then characterized by fluctuations in eutrophic and oligotrophic taxa (Fig. 9), clearly linked to nutrient availability, in warmer SSTs, as suggested by the marked increases in *Discoaster* and *E. formosa*. A similar shift from oligotrophic to eutrophic conditions has also been identified at Alano Section (Luciani et al., 2010; Toffanin et al., 2011) and in the Southern Ocean (Villa et al., 2014). After the MECO, the decreasing trend of warm-water taxa reflects the cooling trend that characterizes the middle late Eocene (Zachos et al., 2008). Above the acme of the *C. erbae* and the subsequent collapse of this genus, the progressive decline of warm-water and oligotrophic taxa continued. Assemblages remained mostly characterized by warm-water taxa and were enriched with mesotrophic taxa linked to subsequent changes in the nutrient level up to the base of the range of *I. recurvus*. Increased abundances of species adapted to colder and medium-to-rich nutrient waters indicate a gradual cooling of SST that began at the base of the range of *I. recurvus*. The DEE marked the definitive prevalence of cool eu-mesotrophic forms. During the late Eocene the gradual reduction of the stratification of the water column (Tori et al., 2008) and the cooling of SST seem to be the cause of the *Discoaster* crisis, which were deep dwellers taxa (Aubry, 1992). The interval spanning the EOT~~, and the Oi-1 event~~ is characterized by a sudden turnover toward dominantly meso-eutrophic taxa (*Clausicoccus, D. scrippsae, R. dictyoda* and *C. pelagicus*), and an increase in abundance of *R. daviesii, Blackites* spp. and *Clausicoccus* spp. in response to changing SST and nutrient supply (Coccioni et al., 2008; Villa et al., 2008, 2014). Calcareous nannofossils show a significant reorganization of the assemblages with the replacement of the dominant genera, a gradual decrease in species diversity, a decrease in the abundance of warm-water taxa (*Discoaster* and *Sphenolithus*), and the collapse of oligotrophic taxa (*Cribrocentrum, R. umbilicus, Discoaster,* and *E. formosa*). All these changes seem to be mainly related to a gradual (step-by-step) eutrophication, environmental instability, and small changes of SST.

Thus, the high-resolution record of calcareous nannofossil reported here clearly suggests a loss of stratification, increased instability, and general eutrophication trend in the water column during this time interval. Nutrient enrichment shows a stable trend starting at ~37 Ma, therefore preceding the water cooling. This may mean that first there was a generalized loss of stratification in the water column and, later, a decrease of SST. All these changes could be related to an increase in seasonality, carbon cycle variability, and also to modification in oceanic circulation. Furthermore, the increased abundance of *Z. bijugatus* and *L. minutus*, known as shallow-water taxa, corroborates the sea level shallowing assumed by the increasing terrigenous/carbonate ratio interpreted from high MS values in the upper part of the section.

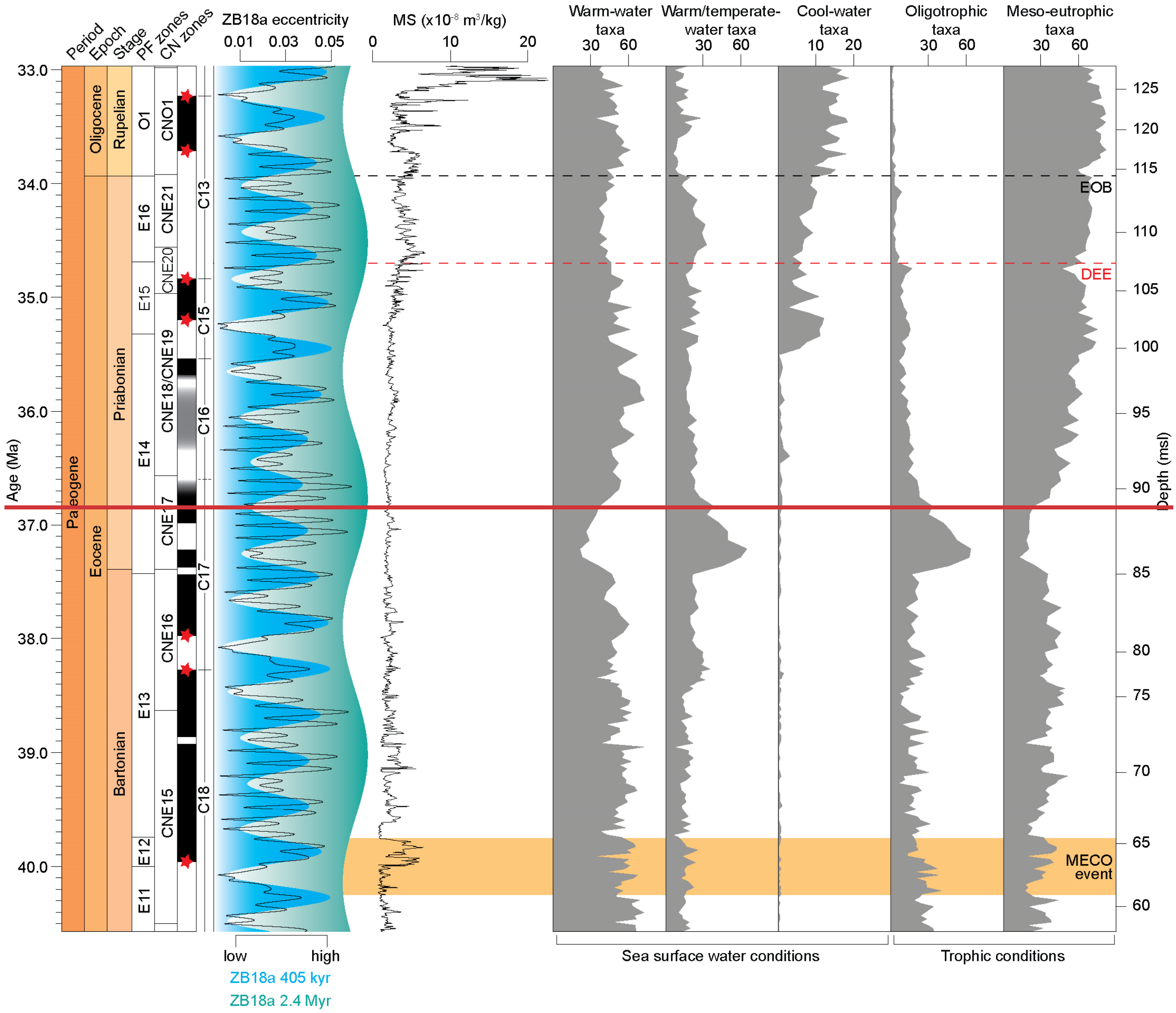
Period
Epoch
Stage
PF zones
CN zones
ZB18a eccentricity
0.01 0.03 0.05
MS (x10⁻⁸ m³/kg)
0 10 20
Warm-water taxa
30 60
Warm/temperate-water taxa
30 60
Cool-water taxa
10 20
Oligotrophic taxa
30 60
Meso-eutrophic taxa
30 60
Age (Ma)
33.0
34.0
35.0
36.0
37.0
38.0
39.0
40.0
Paleogene
Oligocene
Eocene
Rupelian
Priabonian
Bartonian
O1
E16
E15
E14
E13
E12
E11
CNO1
CNE21
CNE20
CNE18/CNE19
CNE17
CNE16
CNE15
C13
C15
C16
C17
C18
EOB
DEE
MECO event
Depth (msl)
125
120
115
110
105
100
95
90
85
80
75
70
65
60
low
high
ZB18a 405 kyr
ZB18a 2.4 Myr
Sea surface water conditions
Trophic conditions

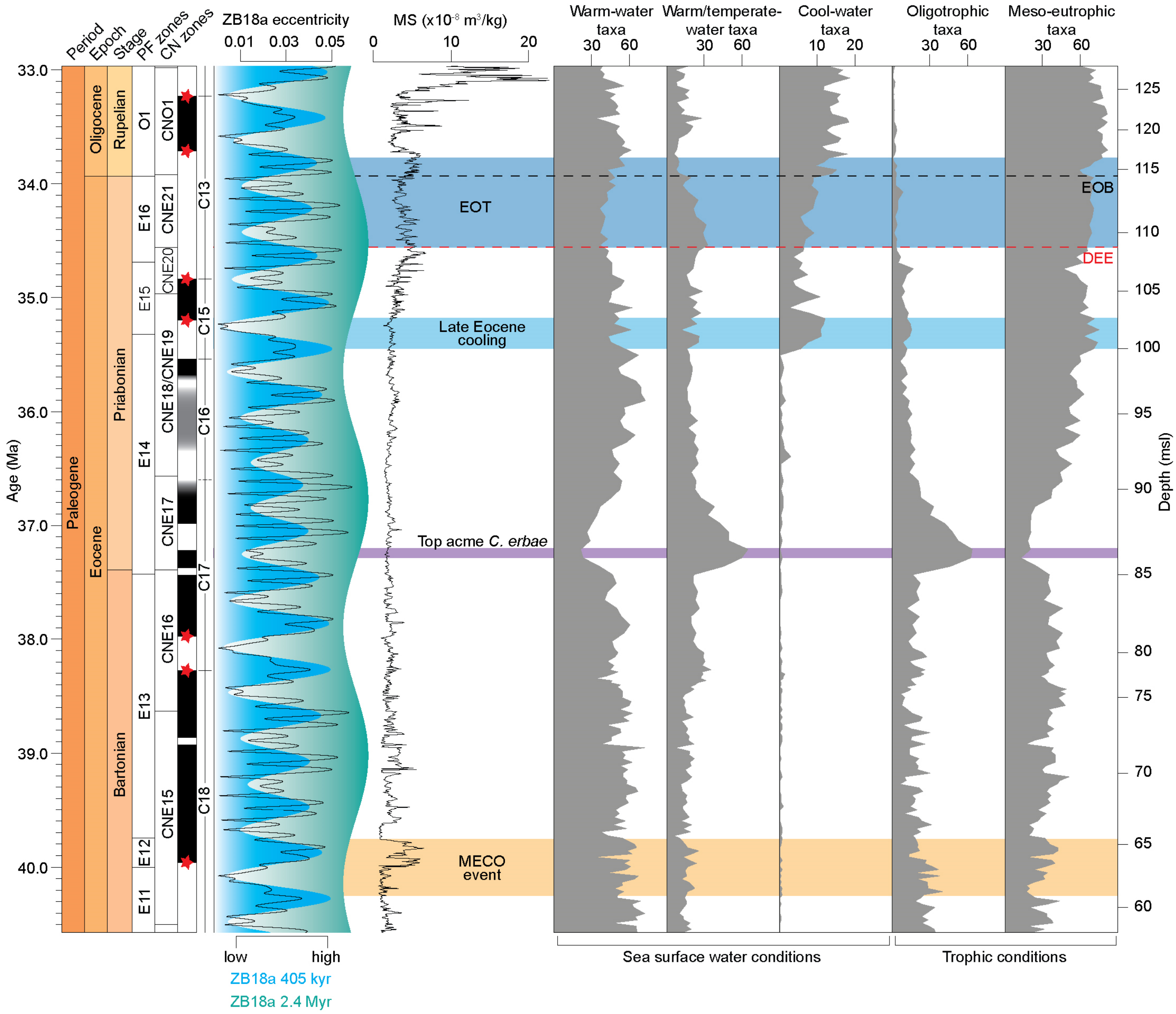

Figure 9. Astrochronology time scale of the MCA Section established by 405 kyr tuning and groups of paleoenvironmentally significant calcareous nannofossils. From left to right: Planktonic foraminiferal (PF; Jovane et al., 2013) and calcareous nannofossil (CN; this study) biozonation following the schemes proposed by Wade et al. (2011) and Agnini et al. (2014), magnetostratigraphic interpretation after Jovane et al. (2013) with the most reliable magnetic polarity reversals indicated by red stars, ZB18a astronomical solution (Zeebe and Lourens, 2019) with the 405 kyr (blue area) and the 2.4 Myr (green area) components, MS record, and the relative abundance (%) of calcareous nannofossil groups (Table 2; Notice the scale difference for the cool-water taxa). Black and red horizontal dashed lines indicate the Eocene-Oligocene boundary (EOB) and the *Discoaster* extinction event (DEE), respectively. Dark blue interval indicates the EOT as a ~790 kyr

event started at the extinction of *D. saipanensis* (Hutchinson et al., 2021). Light blue interval indicates the late Eocene cooling showed by calcareous nannofossil cool-water taxa. Purple interval indicates the top acme of *C. erbae*, which marks the onset of the oligotrophic taxa decreasing trend. ~~The o~~Orange interval indicates the MECO based on its stratigraphic constraint as proposed by Savian et al. (2014). Warm-water taxa comprehend *Sphenolithus* spp., *D. scrippsae, C. pelagicus,* and *Discoaster* spp.; warm/temperate-water taxa comprehend *E. formosa*, *D. bisectus*, *Z. bijugatus*, *Cribrocentrum* spp., and *L. minutus*; cool water taxa comprehend *Blackites* spp*., C. protoannulus, R. daviesii, Clausicoccus* spp., and *Helicosphaera+Pontosphaera*; oligotrophic water taxa comprehend *Cribrocentrum* spp., *C. eopelagicus, R. umbilicus, Discoaster* spp*., C. protoannula,* and *E. formosa*; and meso-eutrophic water taxa comprehend *Clausicoccus* spp., *D. scrippsae, R. dyctioda* group, *C. pelagicus, Blackites* spp., *L. minutus,* and *D. bisectus*.

5.4. Timing of the MECO event in the MCA Section

The MECO is recognized as one of the most ~~rapid~~ enigmatic warming events of the Cenozoic, probably related to $p\mathrm{CO_2}$ global changes (Bohaty and Zachos, 2003). Its duration was firstly estimated to last over than 600 kyr (Bohaty and Zachos, 2003), but the recently estimated duration decreased to about 500 kyr, with the peak warming lasting less than 100 kyr and placed around 40.0 Ma (Bohaty et al., 2009). Savian et al. (2014) ~~identified and placed~~recognized the stratigraphic interval corresponding to the MECO event in the MCA Section ~~between approximately 61.0 and 65.5 msl~~ based on a multi-proxy study. Micropaleontology, geochemistry, rock magnetic, and stable isotope data, constrained by bio- and magnetostratigraphic datums, allowed them to place the entire event between ~61.0 and ~65.5 msl and the peak warming together with its aftermath specifically between ~63.2 and ~65.5 msl. In addition to micropaleontological and geochemical evidence, Savian et al. (2014) reported increased aeolian iron supply and enhanced putative magnetofossil concentrations within this shorter interval, which altogether was interpreted as a period of high primary productivity. Our age model allowed us to place this interval in time domain and compare it with other records in which MECO was identified. Based on the MECO constraint from Savian et al. (2014), together with our developed age model, we have been able to place the event approximately between 40.24 and 39.75 Ma (Fig. 10), which supports the duration of about 500 kyr with peak warming occurring~~ed~~ around 40.0 Ma. Besides, it consistently agrees with the recent placing of MECO event in the Neo-Tethys (Giorgioni et al., 2019).

Our study also ~~points out~~highlights the importance of the orbital forcing influencing the MECO climate warming due to its coincidence with a node of lows in the 405 kyr and 2.4 Myr components of eccentricity, as firstly suggested by Westerhold and Röhl (2013). Giorgioni et al. (2019) already showed the same behavior in the Neo-Tethys, and here we demonstrate it again for the MCA Section (Fig. 10). As discussed by Giorgioni et al. (2019), this orbital forcing could have enhanced the effects of the India-Asia collisional event in the Tethys (Jovane et al., 2009; Najaman et al., 2010), functioning as a trigger for climate warming and carbon cycle instability.

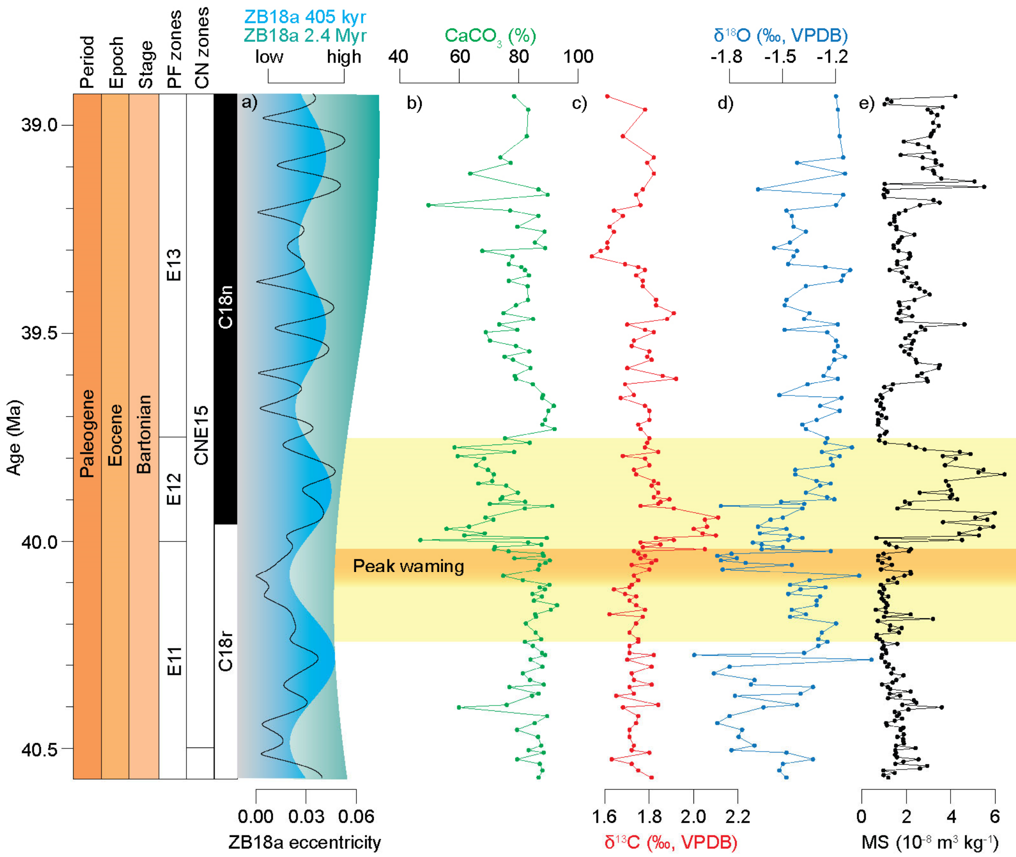

Figure 10. The MECO event (yellow) at the MCA Section with peak warming defined as the negative $\delta^{18}O$ anomaly (orange). a) ZB18a astronomical solution (Zeebe and Lourens, 2019) with the

2.4 Myr and the 405 kyr cycles extracted by a Gaussian bandpass filter centered at 0.00042 ± 0.00004 kyr^{-1} and 0.002469 ± 0.0006 kyr^{-1}, respectively. b-e) $CaCO_3$, $\delta^{13}C$, $\delta^{18}O$ and MS data from Savian et al. (2014). Magnetostratigraphic interpretation is from Jovane et al. (2013). Planktonic foraminiferal (PF; Jovane et al., 2013) and calcareous nannofossil (CN; this study) biozonation following the schemes proposed by Wade et al. (2011) and Agnini et al. (2014), respectively.

6. Conclusions

Based on previous studies of correlated sections, marls and limestones at the MCA Section are inferred to have been deposited during warm/wet and cold/dry intervals, respectively. Together with a radiometric date and magneto- and biostratigraphic tie points, we were able to construct a new high-resolution age model for the MCA Section, by tuning the minima in the identified long eccentricity cycle of the MS record to minima in the astronomical solution. Our orbitally tuned age model allowed us to place the base of the Priabonian stage in the MCA Section at ~37.4 Ma, based on the identification of the base of common *C. erbae*, and to independently confirm the base of the Rupelian stage at ~33.9 Ma, as previously suggested. We constrained the MECO event duration to be ~500 kyr with its peak warmth at ~40.0 Ma, coinciding with a minimum in the 2.4 Myr and 405 kyr eccentricity components, also corroborating previous studies. The developed age model also points out the necessity of revisiting the MCA magnetostratigraphy, particularly between chrons C18n to C15r. Calcareous nannofossil paleoenvironmentally significant groups allowed the identification of a gradual eutrophication with an abrupt change ~~dominance reversal~~ from oligotrophic to eutrophic conditions at around 37 Ma. Assemblages show that nutrient enrichment preceded water cooling at the late Eocene, suggesting that, prior to the cooling, a loss of water column stratification took place. Furthermore, we strongly reinforce the need for a study within the EOT interval at the MCA Section with high-resolution isotopic records in order to constrain important events such as the Oi-1 based on isotopic signature. Despite these, the MCA is a continuous section in the hundreds of thousand years scale, spanning the late Eocene through the early Oligocene. Therefore, it has the potential to become instrumental in understanding major paleoceanographic and paleoclimatic changes during this interval, over important events such as the MECO and the EOT.

Acknowledgments

We thank the Paleomagnetic Laboratory of National Oceanography Centre Southampton (NOCS) for the use of equipment facilities. MK is supported by the Conselho Nacional de Desenvolvimento Científico e Tecnológico (CNPq – grant number 132076/2019-5). JFS is also supported by the CNPq (grant number 201508/2009-5) and Fundação de Amparo à Pesquisa do Estado do Rio Grande do Sul (FAPERGS – grant number 16/2551-0000213-4). SM and FT are supported by MIUR-PRIN (grant number 2007W9B2WE) and the University of Florence. We are very grateful to Editor Alex Dickson, Slah Boulila, and an anonymous reviewer for their detailed and constructive comments that considerably helped us to improve the manuscript.

References

Agnini, C., Backman, J., Boscolo-Galazzo, F., Condon, D.J., Fornaciari, E., Galeotti, S., Giusberti, L., Grandesso, P., Lanci, L., Luciani, V., Monechi, S., Muttoni, G., Pälike, H., Pampaloni, M.L., Papazzoni, C.A., Pearson, P.N., Pignatti, J., Silva, I.P., Raffi, I., Rio, D., Rook, L., Sahy, D., Spofforth, D.J.A., Stefani, C., Wade, B.S., 2020. Proposal for the Global Boundary Stratotype Section and Point (GSSP) for the Priabonian Stage (Eocene) at the Alano section (Italy). Episodes. https://doi.org/10.18814/epiiugs/2020/020074

Agnini, C., Fornaciari, E., Giusberti, L., Grandesso, P., Lanci, L., Luciani, V., Muttoni, G., Palike, H., Rio, D., Spofforth, D.J.A., Stefani, C., 2011. Integrated biomagnetostratigraphy of the Alano section (NE Italy): A proposal for defining the middle-late Eocene boundary. Geol. Soc. Am. Bull. 123, 841–872. https://doi.org/10.1130/B30158.1

Agnini, C., Fornaciari, E., Raffi, I., Catanzariti, R., Pälike, H., Backman, J., Rio, D., 2014. Biozonation and biochronology of Paleogene calcareous nannofossils from low and middle latitudes. Newsletters Stratigr. 47, 131–181. https://doi.org/10.1127/0078-0421/2014/0042

Allen, M.B., Armstrong, H.A., 2008. Arabia-Eurasia collision and the forcing of mid-Cenozoic global cooling. Palaeogeogr. Palaeoclimatol. Palaeoecol. 265, 52–58. https://doi.org/10.1016/j.palaeo.2008.04.021

Angori, E., Bernaola, G., Monechi, S., 2007. Calcareous nannofossil assemblages and their response to the Paleocene-Eocene Thermal Maximum event at different latitudes: ODP Site 690 and Tethyan sections, in: Large Ecosystem Perturbations: Causes and Consequences. Geological Society of America. https://doi.org/10.1130/2007.2424(04)

Aubry, M.-P., 1992. 13. Late Paleogene Calcareous Nannoplankton Evolution: A Tale of Climatic Deterioration, in: Prothero, D.R., Berggren, W.A. (Eds.), Eocene-Oligocene Climatic and Biotic Evolution. Princeton University Press, Princeton, pp. 272–309. https://doi.org/10.1515/9781400862924.272

Barker, P.F., Filippelli, G.M., Florindo, F., Martin, E.E., Scher, H.D., 2007. Onset and role of the Antarctic Circumpolar Current. Deep Sea Res. Part II Top. Stud. Oceanogr. 54, 2388–2398. https://doi.org/10.1016/j.dsr2.2007.07.028

Bohaty, S.M., Zachos, J.C., 2003. Significant Southern Ocean warming event in the late middle Eocene. Geology 31, 1017. https://doi.org/10.1130/G19800.1

Bohaty, S.M., Zachos, J.C., Florindo, F., Delaney, M.L., 2009. Coupled greenhouse warming and deep-sea acidification in the middle Eocene. Paleoceanography 24, n/a-n/a. https://doi.org/10.1029/2008PA001676

Boulila, S., Galbrun, B., Hinnov, L.A., Collin, P.-Y., 2008a. High-resolution cyclostratigraphic analysis from magnetic susceptibility in a Lower Kimmeridgian (Upper Jurassic) marl–

limestone succession (La Méouge, Vocontian Basin, France). Sediment. Geol. 203, 54–63. https://doi.org/10.1016/j.sedgeo.2007.10.004

Boulila, S., Galbrun, B., Hinnov, L.A., Collin, P.-Y., 2008b. Orbital calibration of the Early Kimmeridgian (southeastern France): implications for geochronology and sequence stratigraphy. Terra Nov. 20, 455–462. https://doi.org/10.1111/j.1365-3121.2008.00838.x

Boulila, S., Hinnov, L.A., Huret, E., Collin, P.-Y., Galbrun, B., Fortwengler, D., Marchand, D., Thierry, J., 2008c. Astronomical calibration of the Early Oxfordian (Vocontian and Paris basins, France): Consequences of revising the Late Jurassic time scale. Earth Planet. Sci. Lett. 276, 40–51. https://doi.org/10.1016/j.epsl.2008.09.006

Boulila, S., Vahlenkamp, M., De Vleeschouwer, D., Laskar, J., Yamamoto, Y., Pälike, H., Kirtland Turner, S., Sexton, P.F., Westerhold, T., Röhl, U., 2018. Towards a robust and consistent middle Eocene astronomical timescale. Earth Planet. Sci. Lett. 486, 94–107. https://doi.org/10.1016/j.epsl.2018.01.003

Bown, P.R., Young, J.R., 1998. Introduction — calcareous nannoplankton biology, in: Bown, P.R. (Ed.), Calcareous Nannofossil Biostratigraphy. Chapman and Hall, London, pp. 1–15.

Bralower, T.J., 2002. Evidence of surface water oligotrophy during the Paleocene-Eocene thermal maximum: Nannofossil assemblage data from Ocean Drilling Program Site 690, Maud Rise, Weddell Sea. Paleoceanography 17, 13-1-13–12. https://doi.org/10.1029/2001PA000662

Bukry, D., 1981. Pacific Coast Coccolith Stratigraphy between Point Conception and Cabo Corrientes, Deep Sea Drilling Project Leg 63, in: Initial Reports of the Deep Sea Drilling Project, 63. U.S. Government Printing Office. https://doi.org/10.2973/dsdp.proc.63.111.1981

Cande, S.C., Kent, D. V., 1995. Revised calibration of the geomagnetic polarity timescale for the Late Cretaceous and Cenozoic. J. Geophys. Res. Solid Earth 100, 6093–6095. https://doi.org/10.1029/94JB03098

Carminati, E., Doglioni, C., 2012. Alps vs. Apennines: The paradigm of a tectonically asymmetric Earth. Earth-Science Rev. 112, 67–96. https://doi.org/10.1016/j.earscirev.2012.02.004

Coccioni, R., Marsili, A., Montanari, A., Bellanca, A., Neri, R., Bice, D.M., Brinkhuis, H., Church, N., Macalady, A., McDaniel, A., Deino, A., Lirer, F., Sprovieri, M., Maiorano, P., Monechi, S., Nini, C., Nocchi, M., Pross, J., Rochette, P., Sagnotti, L., Tateo, F., Touchard, Y., Van Simaeys, S., Williams, G.L., 2008. Integrated stratigraphy of the Oligocene pelagic sequence in the Umbria-Marche basin (northeastern Apennines, Italy): A potential Global Stratotype Section and Point (GSSP) for the Rupelian/Chattian boundary. Bull. Geol. Soc. Am. 120, 487–511. https://doi.org/10.1130/B25988.1

Coccioni, R., Montanari, A., Bice, D., Brinkhuis, H., Deino, A., Frontalini, F., Lirer, F., Maiorano, P., Monechi, S., Pross, J., Rochette, P., Sagnotti, L., Sideri, M., Sprovieri, M., Tateo, F., Touchard, Y., Van Simaeys, S., Williams, G., 2018. The Global Stratotype Section and Point (GSSP) for the base of the Chattian Stage (Paleogene System, Oligocene Series) at Monte Cagnero, Italy. Episodes 41, 17–32. https://doi.org/10.18814/epiiugs/2018/v41i1/018003

Coccioni, R., Sideri, M., Bancalà, G., Catanzariti, R., Frontalini, F., Jovane, L., Montanari, A., Savian, J., 2013. Integrated stratigraphy (magneto-, bio- and chronostratigraphy) and geochronology of the Palaeogene pelagic succession of the Umbria–Marche Basin (central Italy). Geol. Soc. London, Spec. Publ. 373, 111–131. https://doi.org/10.1144/SP373.4

Coxall, H.K., Wilson, P.A., Pälike, H., Lear, C.H., Backman, J., 2005. Rapid stepwise onset of Antarctic glaciation and deeper calcite compensation in the Pacific Ocean. Nature 433, 53–57. https://doi.org/10.1038/nature03135

Davis, J.C., Sampson, R.J., 1986. Statistics and Data Analysis in Geology, 2nd ed. John Wiley & Sons, New York.

DeConto, R.M., Pollard, D., 2003. Rapid Cenozoic glaciation of Antarctica induced by declining atmospheric CO2. Nature 421, 245–249. https://doi.org/10.1038/nature01290

Doglioni, C., Bosellini, A., 1987. Eoalpine and mesoalpine tectonics in the Southern Alps. Geol. Rundschau 76, 735–754. https://doi.org/10.1007/BF01821061

Dunkley Jones, T., Bown, P.R., Pearson, P.N., Wade, B.S., Coxall, H.K., Lear, C.H., 2008. Major shifts in calcareous phytoplankton assemblages through the Eocene-Oligocene transition of Tanzania and their implications for low-latitude primary production. Paleoceanography 23, n/a-n/a. https://doi.org/10.1029/2008PA001640

Fioroni, C., Villa, G., Persico, D., Jovane, L., 2015. Middle Eocene-Lower Oligocene calcareous nannofossil biostratigraphy and paleoceanographic implications from Site 711 (equatorial Indian Ocean). Mar. Micropaleontol. 118, 50–62. https://doi.org/10.1016/j.marmicro.2015.06.001

Fornaciari, E., Agnini, C., Catanzariti, R., Rio, D., Bolla, E.M., Valvasconi, E., 2010. Mid-latitude calcareous nannofossil biostratigraphy and biochronology across the middle to late Eocene transition. Stratigraphy 7, 229–264.

Galeotti, S., DeConto, R., Naish, T., Stocchi, P., Florindo, F., Pagani, M., Barrett, P., Bohaty, S.M., Lanci, L., Pollard, D., Sandroni, S., Talarico, F.M., Zachos, J.C., 2016. Antarctic Ice Sheet variability across the Eocene-Oligocene boundary climate transition. Science (80-.). 352, 76–80. https://doi.org/10.1126/science.aab0669

Galeotti, S., Sahy, D., Agnini, C., Condon, D., Fornaciari, E., Francescone, F., Giusberti, L., Pälike, H., Spofforth, D.J.A., Rio, D., 2019. Astrochronology and radio-isotopic dating of the Alano di Piave section (NE Italy), candidate GSSP for the Priabonian Stage (late Eocene). Earth Planet. Sci. Lett. 525, 115746. https://doi.org/10.1016/j.epsl.2019.115746

Gardin, S., Monechi, S., 1998. Palaeoecological change in middle to low latitude calcareous nannoplankton at the Cretaceous/Tertiary boundary. Bull. la Société Géologique Fr. 169, 709–723.

Gibbs, S.J., Bown, P.R., Sessa, J.A., Bralower, T.J., Wilson, P.A., 2006. Nannoplankton Extinction and Origination Across the Paleocene-Eocene Thermal Maximum. Science (80-.). 314, 1770–1773. https://doi.org/10.1126/science.1133902

Giorgioni, M., Jovane, L., Rego, E.S., Rodelli, D., Frontalini, F., Coccioni, R., Catanzariti, R., Özcan, E., 2019. Carbon cycle instability and orbital forcing during the Middle Eocene Climatic Optimum. Sci. Rep. 9, 9357. https://doi.org/10.1038/s41598-019-45763-2

Gouhier, T.C., Grinsted, A., Simko, V., 2019. R package biwavelet: Conduct Univariate and Bivariate Wavelet Analyses.

Gradstein, F.M., Ogg, J.G., Schmitz, M.D., Ogg, G.M., 2012. The Geologic Time Scale 2012. Elsevier.

Grinsted, A., Moore, J.C., Jevrejeva, S., 2004. Application of the cross wavelet transform and wavelet coherence to geophysical time series. Nonlinear Process. Geophys. 11, 561–566. https://doi.org/10.5194/npg-11-561-2004

Guerrera, F., Monaco, P., Nocchi, M., Parisi, G., Franchi, R., Vannucci, S., Giovanninni, G., 1988. La Scaglia Variegata Eocenica nella sezione di Monte Cagnero (bacino marchigiano interno): studio litostratigrafico, petrografico e biostratigrafico. Boll. Soc. Geol. Ital. 81–99.

Hammer, Ø., Harper, D.A.T., Ryan, P.D., 2001. PAST: Paleontological statistics software package for education and data analysis. Palaeontol. Electron. 4.

Haq, B.U., Lohmann, G.P., 1976. Early Cenozoic calcareous nannoplankton biogeography of the Atlantic Ocean. Mar. Micropaleontol. 1, 119–194. https://doi.org/10.1016/0377-8398(76)90008-6

Hilgen, F.J., Lourens, L.J., Van Dam, J.A., Beu, A.G., Boyes, A.F., Cooper, R.A., Krijgsman, W., Ogg, J.G., Piller, W.E., Wilson, D.S., 2012. The Neogene Period, in: The Geologic Time Scale. Elsevier, pp. 923–978. https://doi.org/10.1016/B978-0-444-59425-9.00029-9

Hinnov, L.A., 2013. Cyclostratigraphy and its revolutionizing applications in the earth and planetary sciences. Geol. Soc. Am. Bull. 125, 1703–1734. https://doi.org/10.1130/B30934.1

Hinnov, L.A., 2018. Astronomical metronome of geological consequence. Proc. Natl. Acad. Sci. 115, 6104–6106. https://doi.org/10.1073/pnas.1807020115

Hutchinson, D.K., Coxall, H.K., Lunt, D.J., Steinthorsdottir, M., de Boer, A.M., Baatsen, M., von der Heydt, A., Huber, M., Kennedy-Asser, A.T., Kunzmann, L., Ladant, J.-B., Lear, C.H., Moraweck, K., Pearson, P.N., Piga, E., Pound, M.J., Salzmann, U., Scher, H.D., Sijp, W.P., Śliwińska, K.K., Wilson, P.A., Zhang, Z., 2021. The Eocene–Oligocene transition: a review of marine and terrestrial proxy data, models and model–data comparisons. Clim. Past 17, 269–315. https://doi.org/10.5194/cp-17-269-2021

Hyland, E., Murphy, B., Varela, P., Marks, K., Colwell, L., Tori, F., Monechi, S., Cleaveland, L., Brinkhuis, H., van Mourik, C.A., Coccioni, R., Bice, D., Montanari, A., 2009. Integrated stratigraphic and astrochronologic calibration of the Eocene-Oligocene transition in the Monte Cagnero section (northeastern Apennines, Italy): A potential parastratotype for the Massignano global stratotype section and point (GSSP), in: The Late Eocene Earth—Hothouse, Icehouse, and Impacts. Geological Society of America, pp. 303–322. https://doi.org/10.1130/2009.2452(19)

Jones, A.P., Dunkley Jones, T., Coxall, H., Pearson, P.N., Nala, D., Hoggett, M., 2019. Low-Latitude Calcareous Nannofossil Response in the Indo-Pacific Warm Pool Across the Eocene-Oligocene Transition of Java, Indonesia. Paleoceanogr. Paleoclimatology 34, 1833–1847. https://doi.org/10.1029/2019PA003597

Jovane, L., Coccioni, R., Marsili, A., Acton, G., 2009. The late Eocene greenhouse-icehouse transition: Observations from the Massignano global stratotype section and point (GSSP), in: The Late Eocene Earth—Hothouse, Icehouse, and Impacts. Geological Society of America. https://doi.org/10.1130/2009.2452(10)

Jovane, L., Florindo, F., Coccioni, R., Dinares-Turell, J., Marsili, A., Monechi, S., Roberts, A.P., Sprovieri, M., 2007a. The middle Eocene climatic optimum event in the Contessa Highway section, Umbrian Apennines, Italy. Geol. Soc. Am. Bull. 119, 413–427. https://doi.org/10.1130/B25917.1

Jovane, L., Florindo, F., Sprovieri, M., Pälike, H., 2006. Astronomic calibration of the late Eocene/early Oligocene Massignano section (central Italy). Geochemistry, Geophys. Geosystems 7, n/a-n/a. https://doi.org/10.1029/2005GC001195

Jovane, L., Savian, J.F., Coccioni, R., Frontalini, F., Bancalà, G., Catanzariti, R., Luciani, V., Bohaty, S.M., Wilson, P.A., Florindo, F., 2013. Integrated magnetobiostratigraphy of the middle Eocene–lower Oligocene interval from the Monte Cagnero section, central Italy. Geol. Soc. London, Spec. Publ. 373, 79–95. https://doi.org/10.1144/SP373.13

Jovane, L., Sprovieri, M., Coccioni, R., Florindo, F., Marsili, A., Laskar, J., 2010. Astronomical calibration of the middle Eocene Contessa Highway section (Gubbio, Italy). Earth Planet. Sci. Lett. 298, 77–88. https://doi.org/10.1016/j.epsl.2010.07.027

Jovane, L., Sprovieri, M., Florindo, F., Acton, G., Coccioni, R., Dall'Antonia, B., Dinarès-Turell, J., 2007b. Eocene-Oligocene paleoceanographic changes in the stratotype section, Massignano, Italy: Clues from rock magnetism and stable isotopes. J. Geophys. Res. 112, B11101. https://doi.org/10.1029/2007JB004963

Kennett, J.P., 1977. Cenozoic evolution of Antarctic glaciation, the circum-Antarctic Ocean, and their impact on global paleoceanography. J. Geophys. Res. 82, 3843–3860. https://doi.org/10.1029/JC082i027p03843

Kennett, J.P., Exon, N.F., 2004. Paleoceanographic evolution of the Tasmanian Seaway and its climatic implications. pp. 345–367. https://doi.org/10.1029/151GM19

Kodama, K.P., Hinnov, L.A., 2014. Rock Magnetic Cyclostratigraphy. John Wiley & Sons, Ltd, Oxford. https://doi.org/10.1002/9781118561294

Kotov, S., Pälike, H., 2018. QAnalySeries – a cross-platform time series tuning and analysis tool. https://doi.org/https://doi.org/10.1002/essoar.10500226.1

Ladant, J.-B., Donnadieu, Y., Lefebvre, V., Dumas, C., 2014. The respective role of atmospheric carbon dioxide and orbital parameters on ice sheet evolution at the Eocene-Oligocene transition. Paleoceanography 29, 810–823. https://doi.org/10.1002/2013PA002593

Laskar, J., Fienga, A., Gastineau, M., Manche, H., 2011a. La2010: a new orbital solution for the long-term motion of the Earth. Astron. Astrophys. 532, A89. https://doi.org/10.1051/0004-6361/201116836

Laskar, J., Gastineau, M., Delisle, J.-B., Farrés, A., Fienga, A., 2011b. Strong chaos induced by close encounters with Ceres and Vesta. Astron. Astrophys. 532, L4. https://doi.org/10.1051/0004-6361/201117504

Laskar, J., Robutel, P., Joutel, F., Gastineau, M., Correia, A.C.M., Levrard, B., 2004. A long-term numerical solution for the insolation quantities of the Earth. Astron. Astrophys. 428, 261–285. https://doi.org/10.1051/0004-6361:20041335

Lear, C.H., Bailey, T.R., Pearson, P.N., Coxall, H.K., Rosenthal, Y., 2008. Cooling and ice growth across the Eocene-Oligocene transition. Geology 36, 251. https://doi.org/10.1130/G24584A.1

Li, M., Hinnov, L., Kump, L., 2019b. Acycle: Time-series analysis software for paleoclimate research and education. Comput. Geosci. 127, 12–22. https://doi.org/10.1016/j.cageo.2019.02.011

Li, M., Huang, C., Ogg, J., Zhang, Y., Hinnov, L., Wu, H., Chen, Z.-Q., Zou, Z., 2019a. Paleoclimate proxies for cyclostratigraphy: Comparative analysis using a Lower Triassic marine section in South China. Earth-Science Rev. 189, 125–146. https://doi.org/10.1016/j.earscirev.2019.01.011

Lourens, L.J., Sluijs, A., Kroon, D., Zachos, J.C., Thomas, E., Röhl, U., Bowles, J., Raffi, I., 2005. Astronomical pacing of late Palaeocene to early Eocene global warming events. Nature 435, 1083–1087. https://doi.org/10.1038/nature03814

Luciani, V., Giusberti, L., Agnini, C., Fornaciari, E., Rio, D., Spofforth, D.J.A., Pälike, H., 2010. Ecological and evolutionary response of Tethyan planktonic foraminifera to the middle Eocene climatic optimum (MECO) from the Alano section (NE Italy). Palaeogeogr. Palaeoclimatol. Palaeoecol. 292, 82–95. https://doi.org/10.1016/j.palaeo.2010.03.029

Maiorano, P., Monechi, S., 2006. Early to Late Oligocene calcareous nannofossil bioevents in the Mediterranean (Umbria-Marche basin, central Italy). Riv. Ital. di Paleontol. e Stratigr. 112, 261–273.

Martini, E., 1971. Standard Tertiary and Quaternary calcareous nannoplankton zonation, in: Farinacci, A. (Ed.), Proceedings of the 2nd International Conference on Planktonic Microfossils Roma. Edizione Tecnoscienza, Rome, pp. 739–785.

Messaoud, J.H., Thibault, N., Yaich, C., Monkenbusch, J., Omar, H., Jemai, H.F. Ben, Watkins, D.K., 2020. The Eocene-Oligocene Transition in the South-Western Neo-Tethys (Tunisia): Astronomical Calibration and Paleoenvironmental Changes. Paleoceanogr. Paleoclimatology 35. https://doi.org/10.1029/2020PA003887

~~Meyers, S.R., 2014. Astrochron: An R Package for Astrochronology.~~

Monechi, S., 1986. Calcareous nannofossil events around the Eocene-Oligocene boundary in the Umbrian Appenines (Italy). Palaeogeogr. Palaeoclimatol. Palaeoecol. 57, 61–69. https://doi.org/10.1016/0031-0182(86)90006-4

Monechi, S., Buccianti, A., Gardin, S., 2000. Biotic signals from nannoflora across the iridium anomaly in the upper Eocene of the Massignano section: evidence from statistical analysis. Mar. Micropaleontol. 39, 219–237. https://doi.org/10.1016/S0377-8398(00)00022-0

Najman, Y., Appel, E., Boudagher-Fadel, M., Bown, P., Carter, A., Garzanti, E., Godin, L., Han, J., Liebke, U., Oliver, G., Parrish, R., Vezzoli, G., 2010. Timing of India-Asia collision: Geological, biostratigraphic, and palaeomagnetic constraints. J. Geophys. Res. 115, B12416. https://doi.org/10.1029/2010JB007673

Nyerges, A., Kocsis, Á.T., Pálfy, J., 2020. Changes in calcareous nannoplankton assemblages around the Eocene-Oligocene climate transition in the Hungarian Palaeogene Basin (Central Paratethys). Hist. Biol. 1–14. https://doi.org/10.1080/08912963.2019.1705295

Ogg, J.G., 2012. Geomagnetic Polarity Time Scale, in: Gradstein, F.M., Ogg, James G., Schmitz, M.D., Ogg, G.M. (Eds.), The Geologic Time Scale. Elsevier, pp. 85–113. https://doi.org/10.1016/B978-0-444-59425-9.00005-6

Ogg, J.G., 2020. Geomagnetic Polarity Time Scale, in: Geologic Time Scale 2020. Elsevier, pp. 159–192. https://doi.org/10.1016/B978-0-12-824360-2.00005-X

Ogg, J.G., Smith, A.G., 2004. The geomagnetic polarity time scale, in: Gradstein, F.M., Ogg, J.G., Smith, A.G. (Eds.), A Geologic Timescale. Cambridge University Press, Cambridge, pp. 63–86.

Okada, H., Bukry, D., 1980. Supplementary modification and introduction of code numbers to the low-latitude coccolith biostratigraphic zonation (Bukry, 1973; 1975). Mar. Micropaleontol. 5, 321–325. https://doi.org/10.1016/0377-8398(80)90016-X

Pälike, H., Lyle, M.W., Nishi, H., Raffi, I., Ridgwell, A., Gamage, K., Klaus, A., Acton, G., Anderson, L., Backman, J., Baldauf, J., Beltran, C., Bohaty, S.M., Bown, P., Busch, W., Channell, J.E.T., Chun, C.O.J., Delaney, M., Dewangan, P., Dunkley Jones, T., Edgar, K.M., Evans, H., Fitch, P., Foster, G.L., Gussone, N., Hasegawa, H., Hathorne, E.C., Hayashi, H., Herrle, J.O., Holbourn, A., Hovan, S., Hyeong, K., Iijima, K., Ito, T., Kamikuri, S., Kimoto, K., Kuroda, J., Leon-Rodriguez, L., Malinverno, A., Moore Jr, T.C., Murphy, B.H., Murphy, D.P., Nakamura, H., Ogane, K., Ohneiser, C., Richter, C., Robinson, R., Rohling, E.J., Romero, O., Sawada, K., Scher, H., Schneider, L., Sluijs, A., Takata, H., Tian, J., Tsujimoto, A., Wade, B.S., Westerhold, T., Wilkens, R., Williams, T., Wilson, P.A., Yamamoto, Y., Yamamoto, S., Yamazaki, T., Zeebe, R.E., 2012. A Cenozoic record of the equatorial Pacific carbonate compensation depth. Nature 488, 609–614. https://doi.org/10.1038/nature11360

Pälike, H., Norris, R.D., Herrle, J.O., Wilson, P.A., Coxall, H.K., Lear, C.H., Shackleton, N.J., Tripati, A.K., Wade, B.S., 2006. The Heartbeat of the Oligocene Climate System. Science (80-.). 314, 1894–1898. https://doi.org/10.1126/science.1133822

Parisi, G., Guerrera, F., Madile, M., Magnoni, G., Monaco, P., Monechi, S., Nocchi, M., 1988. Middle Eocene to early Oligocene calcareous nannofossil and foraminiferal biostratigraphy in the Monte Cagnero section, Piobbico (Italy), in: Premoli Silva, I., Coccioni, R., Montanari, A. (Eds.), The Eocene/Oligocene Boundary in the Marche-Umbria Basin (Italy). International Subcommission on Paleogene Stratigraphy, Ancona.

Persico, D., Villa, G., 2004. Eocene–Oligocene calcareous nannofossils from Maud Rise and Kerguelen Plateau (Antarctica): paleoecological and paleoceanographic implications. Mar. Micropaleontol. 52, 153–179. https://doi.org/10.1016/j.marmicro.2004.05.002

Premoli Silva, I., Jenkins, D.G., 1993. Decision on the Eocene-Oligocene boundary stratotype. Episodes 16, 379–382.

Röhl, U., Norris, R.D., Ogg, J.G., 2003. Cyclostratigraphy of upper Paleocene and lower Eocene sediments at Blake Nose Site 1051 (western North Atlantic), in: Causes and Consequences of Globally Warm Climates in the Early Paleogene. Geological Society of America. https://doi.org/10.1130/0-8137-2369-8.567

Röhl, U., Ogg, J.G., Geib, T.L., Wefer, G., 2001. Astronomical calibration of the Danian time scale. Geol. Soc. London, Spec. Publ. 183, 163–183. https://doi.org/10.1144/GSL.SP.2001.183.01.09

Sahy, D., Condon, D.J., Hilgen, F.J., Kuiper, K.F., 2017. Reducing Disparity in Radio-Isotopic and Astrochronology-Based Time Scales of the Late Eocene and Oligocene. Paleoceanography 32, 1018–1035. https://doi.org/10.1002/2017PA003197

Savian, J.F., Jovane, L., Frontalini, F., Trindade, R.I.F., Coccioni, R., Bohaty, S.M., Wilson, P.A., Florindo, F., Roberts, A.P., Catanzariti, R., Iacoviello, F., 2014. Enhanced primary productivity and magnetotactic bacterial production in response to middle Eocene warming in the Neo-Tethys Ocean. Palaeogeogr. Palaeoclimatol. Palaeoecol. 414, 32–45. https://doi.org/10.1016/j.palaeo.2014.08.009

Schneider, L.J., Bralower, T.J., Kump, L.R., 2011. Response of nannoplankton to early Eocene ocean destratification. Palaeogeogr. Palaeoclimatol. Palaeoecol. 310, 152–162. https://doi.org/10.1016/j.palaeo.2011.06.018

Sluijs, A., Zeebe, R.E., Bijl, P.K., Bohaty, S.M., 2013. A middle Eocene carbon cycle conundrum. Nat. Geosci. 6, 429–434. https://doi.org/10.1038/ngeo1807

Speijer, R.P., Pälike, H., Hollis, C.J., Hooker, J.J., Ogg, J.G., 2020. The Paleogene Period, in: Geologic Time Scale 2020. Elsevier, pp. 1087–1140. https://doi.org/10.1016/B978-0-12-824360-2.00028-0

Thomson, D.J., 1982. Spectrum estimation and harmonic analysis. Proc. IEEE 70, 1055–1096. https://doi.org/10.1109/PROC.1982.12433

Toffanin, F., Agnini, C., Fornaciari, E., Rio, D., Giusberti, L., Luciani, V., Spofforth, D.J.A., Pälike, H., 2011. Changes in calcareous nannofossil assemblages during the Middle Eocene Climatic Optimum: Clues from the central-western Tethys (Alano section, NE Italy). Mar. Micropaleontol. 81, 22–31. https://doi.org/10.1016/j.marmicro.2011.07.002

Tori, F., 2008. Variabilità climatica e ciclicità nell’intervallo Eocene Oligocene: dati dai nannofossili calcarei. University of Florence.

Tori, F., Monechi, S., Peck, V.L., Riesselman, C.R., 2008. Multi-proxy sea surface temperature reconstructions from the late Eocene-early Oligocene, Walvis Ridge. Evidence for precursory cooling ~1 million years prior to Oi-1?, in: 33rd International Geological Congress 2008. Norwegian Academy of Science and Letters, Oslo, p. 3283.

~~Torrence, C., Compo, G.P., 1998. A Practical Guide to Wavelet Analysis. Bull. Am. Meteorol. Soc. 79, 61–78. https://doi.org/10.1175/1520-0477(1998)079<0061:APGTWA>2.0.CO;2~~

Tremolada, F., Bralower, T.J., 2004. Nannofossil assemblage fluctuations during the Paleocene–Eocene Thermal Maximum at Sites 213 (Indian Ocean) and 401 (North Atlantic Ocean): palaeoceanographic implications. Mar. Micropaleontol. 52, 107–116. https://doi.org/10.1016/j.marmicro.2004.04.002

Vahlenkamp, M., De Vleeschouwer, D., Batenburg, S.J., Edgar, K.M., Hanson, E., Martinez, M., Pälike, H., MacLeod, K.G., Li, Y.-X., Richter, C., Bogus, K., Hobbs, R.W., Huber, B.T., 2020. A lower to middle Eocene astrochronology for the Mentelle Basin (Australia) and its implications for the geologic time scale. Earth Planet. Sci. Lett. 529, 115865. https://doi.org/10.1016/j.epsl.2019.115865

Villa, G., Fioroni, C., Pea, L., Bohaty, S., Persico, D., 2008. Middle Eocene–late Oligocene climate variability: Calcareous nannofossil response at Kerguelen Plateau, Site 748. Mar. Micropaleontol. 69, 173–192. https://doi.org/10.1016/j.marmicro.2008.07.006

Villa, G., Fioroni, C., Persico, D., Roberts, A.P., Florindo, F., 2014. Middle Eocene to Late Oligocene Antarctic glaciation/deglaciation and Southern Ocean productivity. Paleoceanography 29, 223–237. https://doi.org/10.1002/2013PA002518

Villa, G., Persico, D., 2006. Late Oligocene climatic changes: Evidence from calcareous nannofossils at Kerguelen Plateau Site 748 (Southern Ocean). Palaeogeogr. Palaeoclimatol. Palaeoecol. 231, 110–119. https://doi.org/10.1016/j.palaeo.2005.07.028

Wade, B.S., Pearson, P.N., Berggren, W.A., Pälike, H., 2011. Review and revision of Cenozoic tropical planktonic foraminiferal biostratigraphy and calibration to the geomagnetic polarity and astronomical time scale. Earth-Science Rev. 104, 111–142. https://doi.org/10.1016/j.earscirev.2010.09.003

Wei, W., Villa, G., Wise, S.W.J., 1992. Paleoceanographic Implications of Eocene-Oligocene Calcareous Nannofossils from Sites 711 and 748 in the Indian Ocean, in: Proceedings of the Ocean Drilling Program, 120 Scientific Results. Ocean Drilling Program. https://doi.org/10.2973/odp.proc.sr.120.199.1992

Wei, W., Wise, S.W., 1990. Biogeographic gradients of middle Eocene-Oligocene calcareous nannoplankton in the South Atlantic Ocean. Palaeogeogr. Palaeoclimatol. Palaeoecol. 79, 29–61. https://doi.org/10.1016/0031-0182(90)90104-F

Westerhold, T., Marwan, N., Drury, A.J., Liebrand, D., Agnini, C., Anagnostou, E., Barnet, J.S.K., Bohaty, S.M., De Vleeschouwer, D., Florindo, F., Frederichs, T., Hodell, D.A., Holbourn, A.E., Kroon, D., Lauretano, V., Littler, K., Lourens, L.J., Lyle, M., Pälike, H., Röhl, U., Tian, J., Wilkens, R.H., Wilson, P.A., Zachos, J.C., 2020. An astronomically dated record of Earth's climate and its predictability over the last 66 million years. Science (80-.). 369, 1383–1387. https://doi.org/10.1126/science.aba6853

Westerhold, T., Röhl, U., 2013. Orbital pacing of Eocene climate during the Middle Eocene Climate Optimum and the chron C19r event: Missing link found in the tropical western Atlantic. Geochemistry, Geophys. Geosystems 14, 4811–4825. https://doi.org/10.1002/ggge.20293

Westerhold, T., Röhl, U., Frederichs, T., Bohaty, S.M., Zachos, J.C., 2015. Astronomical calibration of the geological timescale: closing the middle Eocene gap. Clim. Past 11, 1181–1195. https://doi.org/10.5194/cp-11-1181-2015

Westerhold, T., Röhl, U., Laskar, J., Raffi, I., Bowles, J., Lourens, L.J., Zachos, J.C., 2007. On the duration of magnetochrons C24r and C25n and the timing of early Eocene global warming events: Implications from the Ocean Drilling Program Leg 208 Walvis Ridge depth transect. Paleoceanography 22. https://doi.org/10.1029/2006PA001322

Westerhold, T., Röhl, U., Pälike, H., Wilkens, R., Wilson, P.A., Acton, G., 2014. Orbitally tuned timescale and astronomical forcing in the middle Eocene to early Oligocene. Clim. Past 10, 955–973. https://doi.org/10.5194/cp-10-955-2014

Zachos, J.C., Dickens, G.R., Zeebe, R.E., 2008. An early Cenozoic perspective on greenhouse warming and carbon-cycle dynamics. Nature 451, 279–283. https://doi.org/10.1038/nature06588

Zachos, J.C., Quinn, T.M., Salamy, K.A., 1996. High-resolution (104 years) deep-sea foraminiferal stable isotope records of the Eocene-Oligocene climate transition. Paleoceanography 11, 251–266.

Zeebe, R.E., 2017. Numerical Solutions for the Orbital Motion of the Solar System over the Past 100 Myr: Limits and New Results. Astron. J. 154, 193. https://doi.org/10.3847/1538-3881/aa8cce

Zeebe, R.E., Lourens, L.J., 2019. Solar System chaos and the Paleocene–Eocene boundary age constrained by geology and astronomy. Science (80-.). 365, 926–929. https://doi.org/10.1126/science.aax0612